Future Circular Collider

PUBLICATION

Analysis of beam-induced vacuum effects: Deliverable D4.4

Perez Rodriguez, Francisco Jose () *et al.*

30 January 2019

The European Circular Energy-Frontier Collider Study (EuroCirCol) project has received funding from the European Union's Horizon 2020 research and innovation programme under grant No 654305. The information herein only reflects the views of its authors and the European Commission is not responsible for any use that may be made of the information.

The research leading to this document is part of the Future Circular Collider Study

The electronic version of this FCC Publication is available on the CERN Document Server at the following URL :
<http://cds.cern.ch/record/2655286

Grant Agreement No: 654305

EuroCirCol

European Circular Energy-Frontier Collider Study

Horizon 2020 Research and Innovation Framework Programme, Research and Innovation Action

DELIVERABLE REPORT

ANALYSIS OF BEAM-INDUCED VACUUM EFFECTS

Document identifier:	EuroCirCol-P2-WP4-D4.4
Due date:	End of Month 36 (June 1st 2018)
Report release date:	31/05/2018
Work package:	WP4 (Cryogenic beam vacuum system)
Lead beneficiary:	ALBA
Document status:	RELEASED (V1.0)

Abstract:

The vacuum chamber of the FCC-hh will have to cope with unprecedented levels of synchrotron radiation flux and power, dealing at the same time with tighter impedance and magnet aperture requirements. In this new collider the difficulty to maintain an ultra-high vacuum level, essential for a proper operation, increases then considerably compared with the previous collider, the LHC. In this document the beam induced vacuum effects, responsible of the pressure increase, are separately studied. The proposed mitigation measures, at the state of the art, are also discussed. Finally, a comparison of the simulated effects with the measurements taken with the beam screen prototype in the light source is also detailed.

The European Circular Energy-Frontier Collider Study (EuroCirCol) project has received funding from the European Union's Horizon 2020 research and innovation programme under grant No 654305. EuroCirCol began in June 2015 and will run for 4 years. The information herein only reflects the views of its authors and the European Commission is not responsible for any use that may be made of the information.

Delivery Slip

	Name	Partner	Date
Authored by	Francis Perez Paolo Chiggiato Ignasi Bellafont Roberto Kersevan Cedric Garion Vincent Baglin	ALBA CERN	30/04/2018
Edited by	Julie Hadre Johannes Gutleber	CERN	15/05/18
Reviewed by	Michael Benedikt Daniel Schulte	CERN	25/05/18
Approved by	EuroCirCol Coordination Committee		31/05/18

TABLE OF CONTENTS

1. PROBLEM DESCRIPTION 4

2. FCC-HH VACUUM REQUIREMENTS 5

3. SYNCHROTRON RADIATION IN THE FCC-HH 6

4. THE BEAM VACUUM CHAMBER 8

CROSS SECTION 8
PRESSURE AND IMPEDANCE MITIGATION MEASURES 9
BEAM MISALIGNEMENT 12
INTERCONNECTION REGION 13

5. PHOTON RAY TRACING 14

6. BEAM INDUCED EFFECTS 16

PHOTON STIMULATED DESORPTION (PSD) 17
ELECTRON STIMULATED DESORPTION (ESD) 21
ION STIMULATED DESORPTION (ISD) 25

7. MOLECULAR DENSITY PROFILE IN THE ARCS 27

8. EXPECTED HEAT LOAD ON THE COLD MASS 29

9. KARA LIGHT SOURCE EXPERIMENT, LEARNINGS SO FAR 30

10. CONCLUSIONS AND FUTURE WORK SUGGESTIONS 33

11. REFERENCES 34

12. ANNEX GLOSSARY 37

1. PROBLEM DESCRIPTION

The FCC-hh is designed to reach 50 TeV of beam energy, surpassing the 7 TeV frontier that the LHC has established. The higher beam energy generates a much higher level of synchrotron radiation (SR), as compared to the present LHC, bringing the FCC-hh at the level of today's low-energy light sources in terms of SR critical energy, photon flux, and power. The higher photon flux brings, via the photon-stimulated desorption (PSD) effect, a higher gas load, which has to be taken care of in a smaller magnet aperture and with a tighter impedance budget.

Table 1. Comparison of the LHC's and FCC-hh's main parameters concerning the vacuum system

Parameter	**LHC**	**FCC-hh**
Energy [TeV]	7	50
Current [mA]	580	500
Circumference [km]	26.7	100
Dipole magnetic field [T]	8.3	15.8
Photon flux [γ/m/s]	$1 \cdot 10^{17}$	$1.7 \cdot 10^{17}$
SR power [W/m]	0.22	34.6
SR critical energy [eV]	43.8	4238
Cold bore aperture [mm]	50	44
Angle between MB [º]	0.29	0.077
Beam screen inner T [K]	5-20	40-60

This report analyzes the beam induced effects and estimates the impact they would have in the total molecular density level during machine operation. To cope with this phenomena, new, state of art mitigation measures have been proposed, with the idea of ensuring the feasibility of the FCC-hh's vacuum system. Table 1 summarizes the main parameters of the LHC and FCC-hh which concern the vacuum system. The studied beam induced effects, responsible of the pressure increase, are:

- PSD, process where SR photons trigger the desorption of gas molecules from the vacuum chamber when they hit the walls.
- The electron stimulated desorption (ESD), process where electrons, mainly coming from the electron cloud (e-cloud), desorb gas from the chamber walls when impacting against them.
- The ion stimulated desorption (ISD), process where ionized residual gas molecules, due to their carried energy, desorb gas from the chamber walls when impacting against them.

Since the SR and the geometry of the beam screen (BS) play the main role in the development of these phenomena, the BS design has been extensively studied and optimized. It is hereby detailed. Extensive photon ray tracing simulations have also been carried out, and used as an input for the molecular density calculations.

2. FCC-hh VACUUM REQUIREMENTS

Ultra high vacuum (UHV) conditions are normally required in particle colliders to lessen as much as possible the beam distortion by its interaction with the residual gas. The vacuum level is usually expressed in molecular density units, rather than in pressure, because the requirement units of this last term vary with the temperature and it is not directly used in formulas. Two main constraints define the molecular density level which the vacuum system of the FCC-hh has to guarantee:

- The residual gas beam lifetime, > 100 h, same value as in the LHC. The total beam lifetime can be much lower due to other effects [1], nevertheless. Equation 1 expresses this value as a function of the residual gas molecular density.
- The maximum cold mass thermal budget allocated for all the sources ending up on the inside of the cold bore, from the BS. It is < 0.3 W/m per beam, being it ideally < 0.2 W/m for the nuclear scattering contribution alone. These values are dictated by the cooling capacity specifications [2]. Equation 2 expresses the heat load on the cold mass caused by the scattered protons. In Section 8 the total heat load, coming from all the sources, is detailed.

$$\tau_{bg} = \frac{1}{\sigma_g \cdot c \cdot n_g} > 100\ h \tag{1}$$

$$P_c = k_{bs} \cdot \frac{I \cdot E}{c \cdot \tau_{bg}} < 0.2\ W/m \tag{2}$$

Where τ_{bg} is defined as the beam-gas lifetime,
σ_g is the gas cross section, 90 mbarn [3] (hydrogen)
c is the speed of light,
n_g is the molecular density we want to find,
P_c is the scattered power to the cold mass,
k_{bs} is the ratio of the total scattered power absorbed by the cold mass. In the latest design of the vacuum chamber, this value has been found to be around 0.85 as an average along the CELL [4], meaning 15% of the scattered protons are absorbed in the BS. This value corresponds however to a BS geometry subject to iterative optimization, so it might slightly vary in the future.
I is the beam current,
E is the beam's energy.

Using the above equations, we find the value of the molecular density of $1 \cdot 10^{15}$ $H_{2\,eq}/m^3$, where $H_{2\,eq}$ means the equivalent pure H_2 density once the different nuclear scattering cross sections have been taken into account for the other gas species (typically CO, CO_2, CH_4) This calculated density value happens to be the same as that for the LHC.

3. SYNCHROTRON RADIATION IN THE FCC-hh

The SR is expected to be the main source of residual gas in the vacuum chamber, due to the higher SR flux and power as compared to the LHC. As such, the SR has to be studied as much in detail as possible. Even with a lower baseline beam current, the high beam energy which the FCC-hh is intended to achieve increases dramatically the SR critical energy (ε_c) photon flux ($\dot{\Gamma}$), and power (P). These quantities can be expressed with Equations 3, 4, and 5, already given in practical units for protons. They show the strong dependence of beam energy. They are also plotted in Figure 1, alongside with those of the LHC.

$$\dot{\Gamma}\ [\gamma/m/s] = 7.017 \cdot 10^{16} \cdot \frac{E\ [TeV]}{\rho\ [m]} \cdot I\ [mA] \tag{3}$$

$$P\ [W/m] = 1.239 \cdot \frac{E^4\ [TeV]}{\rho^2\ [m]} \cdot I\ [mA] \tag{4}$$

$$\varepsilon_c\ [eV] = 3.583 \cdot 10^2 \cdot \frac{E^3\ [TeV]}{\rho\ [m]} \tag{5}$$

Where $\dot{\Gamma}$ is the photon flux,

P is the emitted power per meter,

ρ is the radius of curvature of the bending magnets,

ε_c is the critical energy.

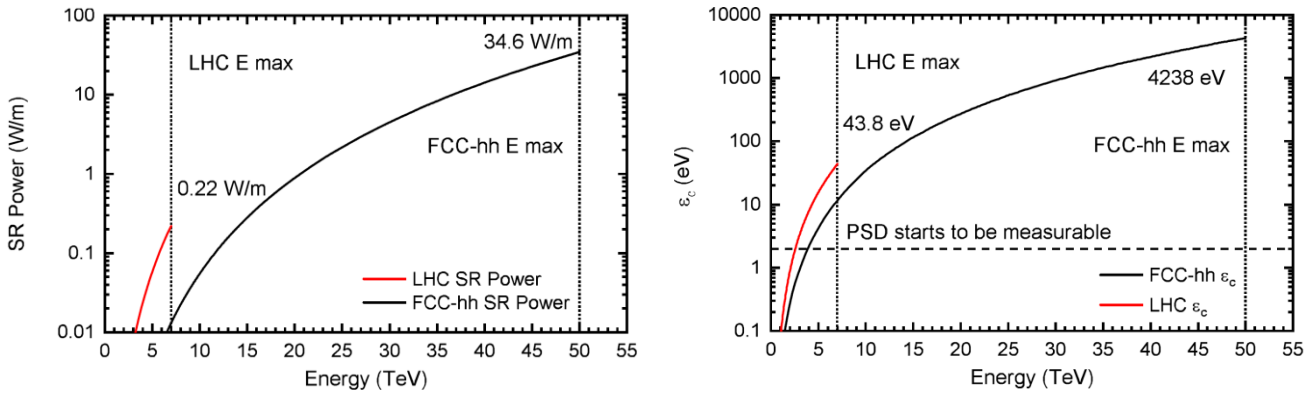

Figure 1. Evolution of the FCC-hh's and the LHC's ε_c and SR power depending on the beam energy. From 0-50 TeV, 15.78 T, 500 mA (FCC-hh) and 0-7 TeV, 8.3 T, 580 mA (LHC)

As it can be appreciated in Figure 1, for the same range of energies valid for the LHC, both the power and ε_c are lower in the case of the FCC-hh because of the dependence on the reciprocal of the bending radius of curvature, which is around 10.57 km in the FCC vs 2.8 km in the LHC. This means that for injection energy, 3.3 TeV baseline, the emitted photon energy will be still too low to trigger any significant observable pressure providing that the chamber's secondary electron yield (SEY) is well below the established multipacting thresholds.

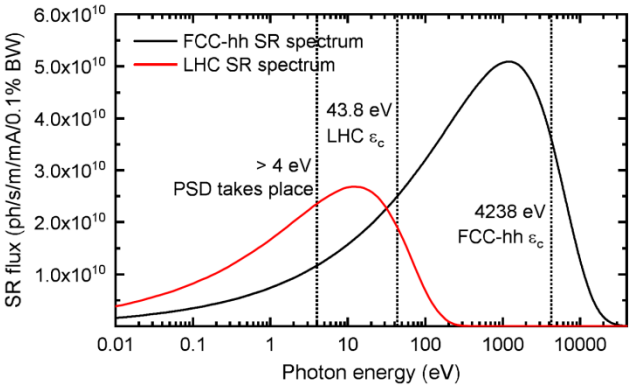

Figure 2. Comparison of the FCC-hh SR spectrum vs the LHC's, highlighting the critical energy values. Data for 50 TeV, 15.78 T (FCC-hh) and 7 TeV, 8.3 T (LHC)

Figure 2 shows a comparison of the SR spectra generated in the two colliders. Whilst in the LHC the main part of the photon flux is generated in the infrared-UV region (0.1-100 eV, 98%), and a marginal part in the soft X-ray region,(> 100 eV, around 2 % of the total flux only), in the case of the FCC-hh around 65 % of the spectrum corresponds to photons with energy > 100 eV corresponding to the soft and hard X rays regions.

It is commonly accepted that the generation of photoelectrons starts from a photon energy of ~ 4 eV, corresponding to the typical work-function value of the materials irradiated by the SR photons (copper, stainless steel). Therefore, photons under this energy won't contribute to the increase of the molecular density inside of the vacuum chamber. In the LHC, for baseline conditions, the flux is $1 \cdot 10^{17}$ ph/s/m, and only 52 % of this amount is above 4 eV. In the FCC-hh, on the other hand, the flux is $1.7 \cdot 10^{17}$ ph/s/m with 88 % of the flux above 4 eV, meaning in fact more than 2.5 times higher effective SR flux.

In addition, the high amount of SR linear power density, 34.6 W/m, rules out the possibility of operating the machine at the LHC's range of temperatures and cooling capacity, making necessary to raise them to improve the cooling efficiency [5]. In Figure 11, in Section 5, a texture map showing the distribution of the SR power along the vacuum chamber is shown, including the SR photon trajectories.

4. THE BEAM VACUUM CHAMBER

CROSS SECTION

The latest beam screen cross section design can be seen in Figure 3, where the chamber layout and surface treatments have been highlighted.

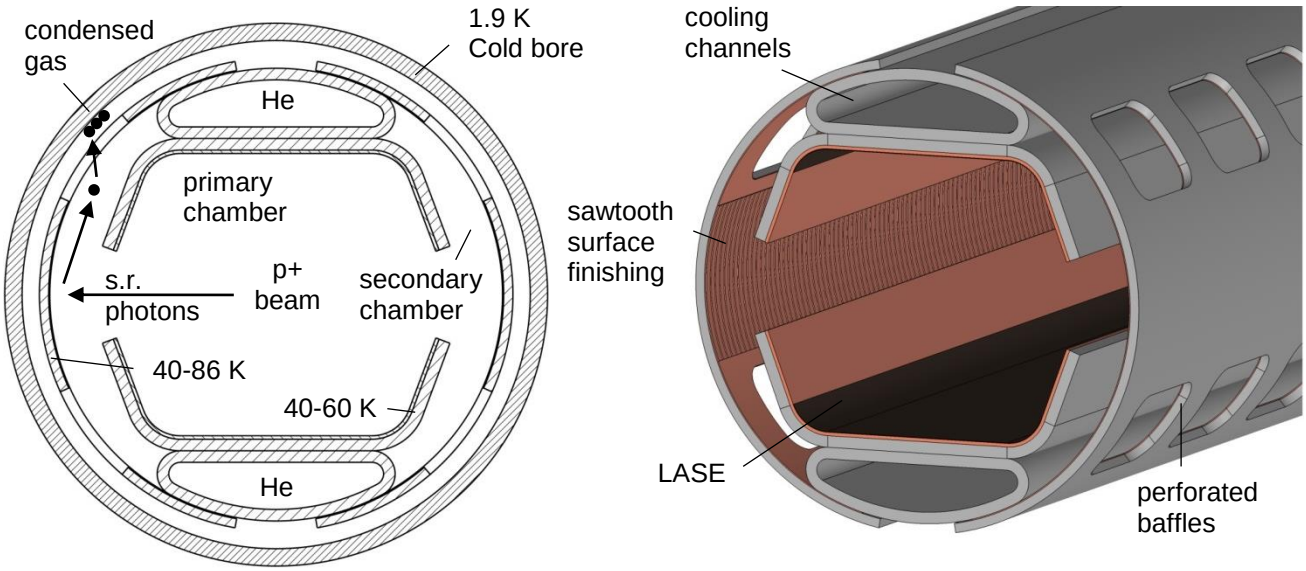

Figure 3. FCC-hh beam screen aimed for bending magnets, showing the LASE treatment of the upper and lower flat areas of the inner chamber

The beam screen design has been already described in a previous document from a mechanical point of view, in the frame of the EuroCirCol project [6], although presenting some differences with respect to the current geometry. Further information about current mechanical features and results can be found in [7]. This design is substantially more complex than the LHC's beam screen. New features have been implemented in order to cope with all the drawbacks derived from the higher beam energy as compared to the LHC. It achieves a higher pumping efficiency than the previous one, as seen in Table 2. Next, the main features of this design aiming to mitigate the beam induced effects will be detailed.

Table 2. Comparison of the LHC's and the FCC-hh's relevant pumping speeds

Parameter	**LHC**	**FCC-hh**
Inner BS temperature range [K]	5-20	40-60
Nominal minimum H_2 pumping speed [l/s/m]	240	800
Normalized H_2 pumping speed at 50 K [l/s/m]	765	844

PRESSURE AND IMPEDANCE MITIGATION MEASURES

In order to mitigate the beam induced effects, while keeping the BS impedance low, a series of design features have been proposed:

- The beam screen has been divided in two chambers, being the most characteristic feature of this new design (see Figure 3). The inner chamber, where the proton beam circulates, has a 0.3 mm thick Cu co-lamination, 4 times thicker than in the LHC, 75 μm. It is kept cold by being in direct contact with the cooling channel and without receiving direct heat load from the SR, keeping the surface properties within an acceptable window for impedance reasons, a parameter of higher importance in this collider as compared to the LHC.

- At the same time, the inner chamber acts as a double-sided shield: on one hand it prevents the larger vertical angle of SR radiation tails to reach the cold bore through the holes, which could rise the heat load on the cold bore and trigger the recycling of the condensed gas species. Screening the holes also keeps the impedance within acceptable levels. Were the inner chamber not present, the Transverse-Mode Coupled Instability (TMCI) budget at injection would be exceeded [8]. On the other hand, it lowers the amount of scattered radiation which is reflected back to the main chamber after hitting the inner area of the secondary one, owing to the narrow aperture. Lowering the amount of radiation reaching the inner chamber area is of the utmost importance, since the electron cloud density is directly proportional to the amount of photoelectrons generated on the surfaces within which the build-up happens.

- Following the LHC example, to minimize the amount of scattered radiation a sawtooth copper surface has been chosen as the element to directly receive and absorb most part of the SR on the BS (Figure 3). Figure 4 shows the teeth profile of a LHC's BS analysed at CERN's metrology lab, showing the valley-peak structure, aimed at intercepting the radiation with perpendicular incidence. Owing to the optical properties of light, the absorption is higher the higher the grazing angle of incidence is. This effect is specially accentuated in the case of X rays, as it can be noticed in

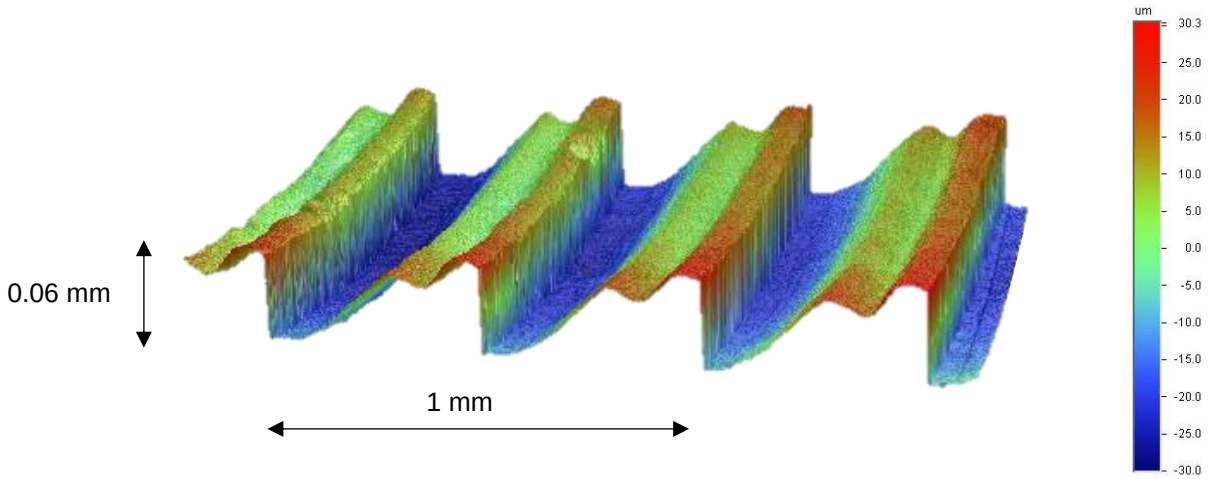

Figure 4. LHC Cu sawtooth surface has measured at CERN's metrology lab with a VEECO optical profilometer

Figure 6. Using the copper reflectivity data displayed on the right, the graph on the left has been obtained. The reflectivity of a flat surface of co-laminated Cu is compared with the same surface with a sawtooth finishing applied. With a perpendicular incidence angle, it can be appreciated that only energies in the UV region and below are reflected, being the reflectivity negligible above 100 eV. The higher amount of SR absorption not only lowers the e-cloud density, but also lowers the outgassing due to the PSD effect (the main pressure source) as the SR is concentrated in areas already conditioned, and

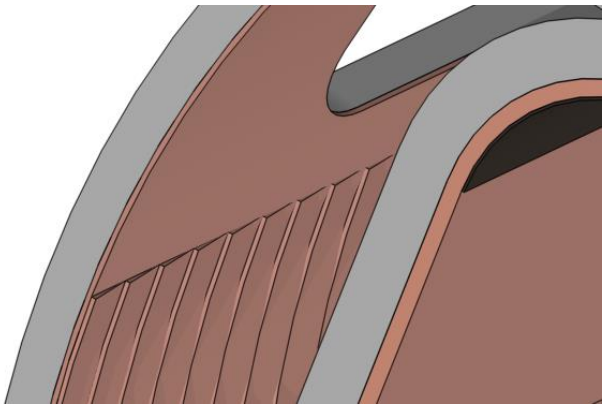

Figure 5. Detail of the sawtooth treatment on the BS's secondary chamber area

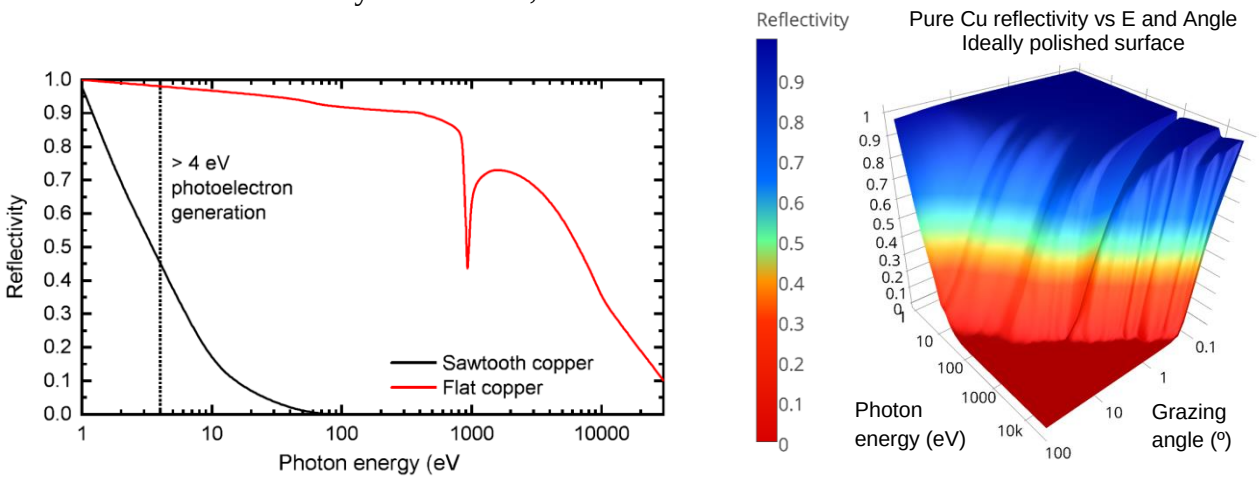

Figure 6. Cu reflectivity compared with ideal sawtooth Cu, for the FCC-hh's average angle of SR incidence, 0.077º

then with lower molecular desorption yield (MDY). Since the sawtooth is to be mechanically applied, a soft metal like copper is necessary. A 0.1 mm thick Cu layer has been chosen for the secondary chamber, also useful to provide enough thermal conductivity in the BS in order to transfer the SR power to the cooling tubes [6, 7]. Figure 5 shows a detail of the sawtooth surface in the BS. It is relevant to mention that LHC's sawtooth geometry must be accurately studied and adapted in the future for the new collider, since the SR grazing angle would be much lower in the FCC-hh than in the LHC (see Table 1). As seen in Figure 4, the teeth are not perfectly triangular. The manufacturing process can leave flat areas on the tip regions which lower the incidence angle of the SR, undesirably increasing the reflectivity and thus the radiation scattering. This increase in the theoretical reflectivity has been recently observed in a dedicated experiment (more information in section 6.2). To decrease the percentage of radiation absorption on these flat areas, apart from improving the manufacturing process, the most effective solution is to reduce the number of teeth, keeping the same constraint of thermal stress at the tooth edge. As an initial approach, doubling the size of the teeth has been proposed, keeping the same ridges angles for simplicity. That being said, for this initial feasibility study the sawtooth has been kept ideal in the simulations. In this case, the power absorption is higher than 99.5%

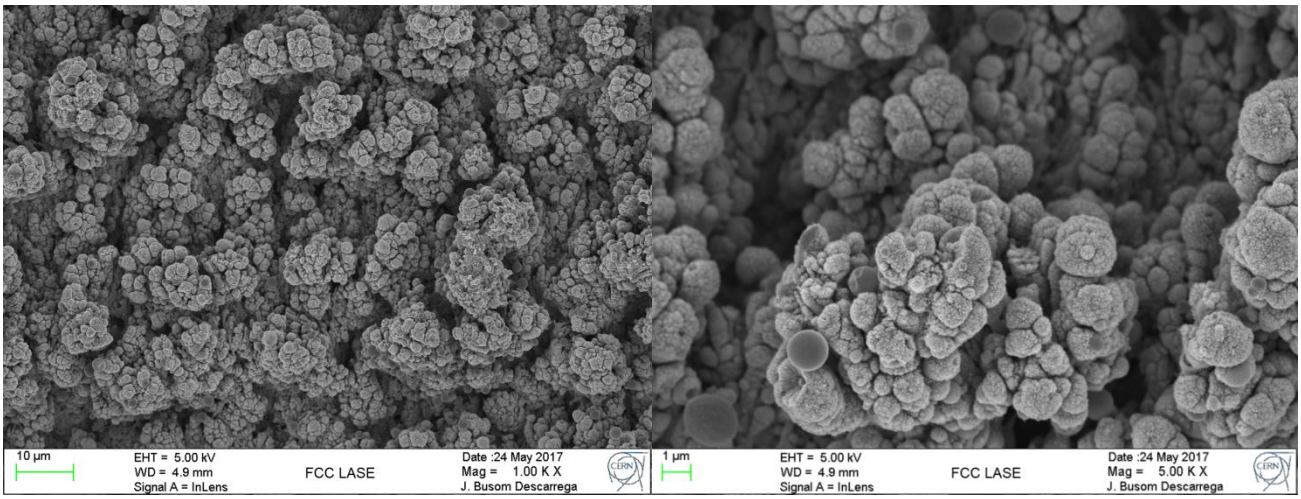

Figure 7. 1.00 K and 5.00 K SEM augmentations of a Cu baseline LASE sample, showing the high roughness and aspect ratio the surface presents, measured at CERN

and more than 90% of the SR flux from the bending magnet (MB) is intercepted by the teeth. As a more expensive and complex alternative, LASE [9, 10] could be also used owing to its good absorption properties [11], even if its original purpose is the SEY mitigation. The high aspect ratio of LASE-treated surface increases a lot the absorption of the original material, effectively giving a better result than the sawtooth finishing. LASE could be applied along the secondary chamber in a continuous strip for a better power dissipation, or just on the flat ridges areas of the sawtooth treatment previously described, if necessary, to counter the effect of a very low grazing angle of incidence. The drawbacks LASE presents, however, are related to its rather poor properties regarding surface impedance, due also to the high surface aspect ratio left by the treatment.

- In order to mitigate SEY and then the e-cloud build-up, it is LASE which has been at the moment chosen from the two initially proposed alternatives [12], because of the possibility of applying it directly in the series manufacturing under atmospheric pressure, lowering then the manufacturing costs, and for its very low SEY values (see Figure 22) which can easily achieve the SEY specifications necessary to avoid critical densities. For this, the critical build-up areas in the inner chamber of the BS are proposed to be treated (see Section 6.2 and Figure 21 for more information). This would allow to reduce the electron density by orders of magnitude under the established instability threshold. Lowering the electron density would also decrease the pressure contribution coming from ESD, placing this effect in a second place, behind the PSD. As a comparison, in the LHC, ESD is contributing to the total pressure for around 90 %, due to the not so low SEY of pure Cu and the low SR critical energy.

- Finally, the design has been optimized to maximize the overall pumping speed, thus lowering the MD contribution coming from all the beam induced effects at the same time. Not being the holes' size an issue for the impedance anymore (as they are geometrically screened), they have been enlarged trying to limit as much as possible the SR leakage to the cold mass. Even if the SR power leakage is negligible, a high amount of flux could lead to the desorption of the condensed gas increasing the pressure over time. Besides, the higher BS temperature (especially in the outgassing areas) further favours the conductance and pumping speed directly, via a dependence with the square root of the

absolute temperature. The resulting pumping speed can be read in Table 2, going for H_2 from 240 l/s/m at 15 K to 844 l/s/m at 50 K, resulting in an increment of 3.5 times compared to the LHC.

BEAM MISALIGNEMENT

The central slot height has been adapted to allow a beam vertical misalignment of 2 mm at 50 TeV beam energy. A too small slot would make the SR beam hit directly the inner chamber, rising its temperature and scattering an excessive amount of radiation which could also induce electron multipacting in the beam region. A too big slot, on the other hand, would mean smaller pumping holes (they should always be placed behind the inner shields, out of the beam sight, as previously mentioned) more radiation leaked to the inner chamber and less pumping speed. As a conservative solution, it has been chosen to fix the central slot height at 7.5 mm, letting pass more than 99% of the total power and more than 90% of the flux, as it can be seen in Figure 8.

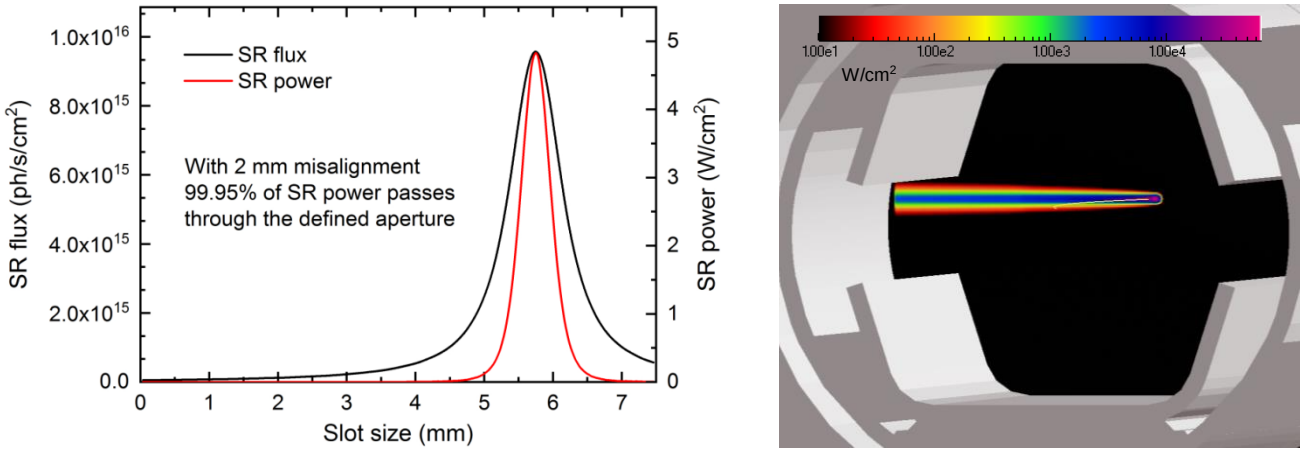

Figure 8. SR beam flux and power baseline distribution, along the central slot (left) and projected on the XY plane (right) passing from the primary chamber (7.5 mm high slot) up to the secondary one. Case of maximum vertical misalignment

In case of injection, at 3.3 TeV, the misalignment could go up to 4 mm, and the emitted SR beam would be much wider (classically, the SR width is defined as ± 1/γ), so a higher amount of flux fraction would touch the inner chamber. Nevertheless, as stated in Section 3, this low energy beam does not produce photons with an energy high enough to have a significant photoelectron generation nor significant SR power (see Equation 4), so no particular detrimental effects are expected with regard to the molecular density level. In case of the impact area, the sawtooth finishing has been designed to be wide enough to cover all the possible irradiated surface.

INTERCONNECTION REGION

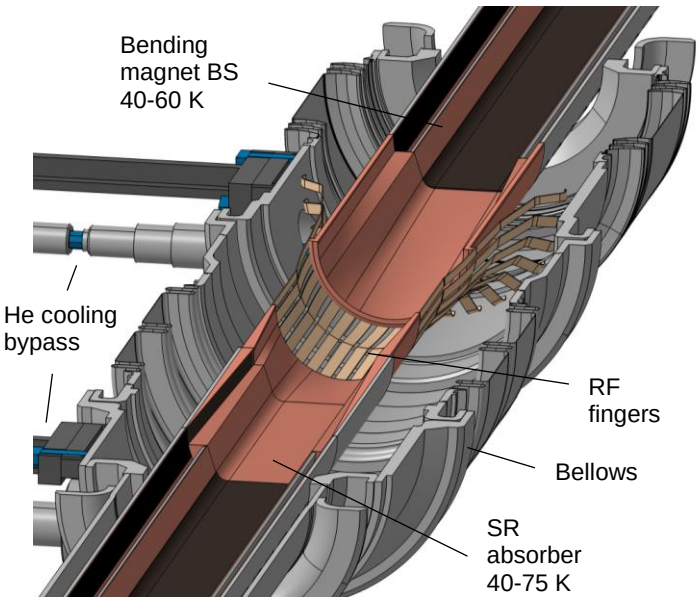

Figure 9. MB interconnect conceptual simplified representation, using LHC's bellows and RF fingers geometry

The interconnections between magnets (see Figures 9 and 10) are the most critical regions in the arcs. All the components have to be assembled with tight tolerances, ensuring good electrical contact between them and minimizing the irradiation of these areas. There is no active cooling because of the He bypass, only conduction cooling leading to a somewhat higher temperature gradient in the area. The absence of distributed pumping, added to the small conductance due to the small dimensions, creates a high pressure peak in this region, which increase considerably the average pressure in the CELL.

The proposed conservative solution to avoid the direct irradiation in this area, is to place one photon absorber at the end of each dipole and short straight section (SSS). This gently tapering geometry (for minimizing the effect on the geometric impedance) absorbs 42 W of SR in the most irradiated magnet, creating a shadow of around 1 m downstream of it, effectively protecting all the elements, and distributing uniformly the radiation on its surface as found in the simulations. To avoid further SR scattering and excessive photoelectron generation in the area without pumping, the surface which receives directly the radiation (the slope depicted in black in the above figure) is recommended to be treated with LASE. In the beginning of the collaboration it was contemplated the possibility of cooling the absorbers with a separate circuit at a higher temperature to improve the cooling efficiency, but the idea was finally discarded owing to the cost increase of the additional circuit. From the vacuum point of view, another solution could be chosen, avoiding the use of the absorber if the second taper (after the RF fingers) had a diameter larger than the outer chamber and the impact area had a photoelectron mitigation treatment (as LASE) to avoid electron multipacting in the irradiated area. This would also require tighter assembling tolerances and could slightly rise the average pressure in the area.

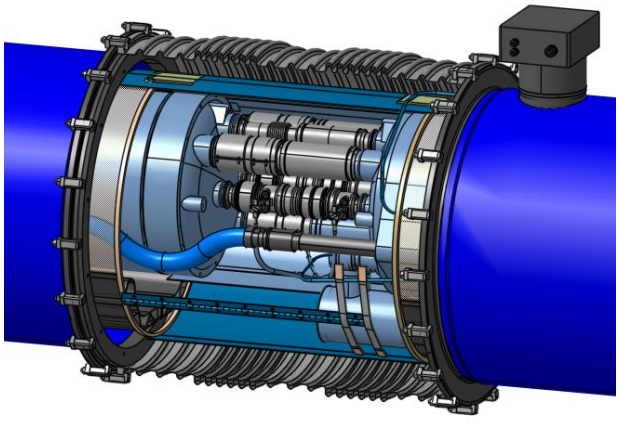

Figure 10. LHC's bending magnet interconnect, from CERN's CAD database

5. PHOTON RAY TRACING

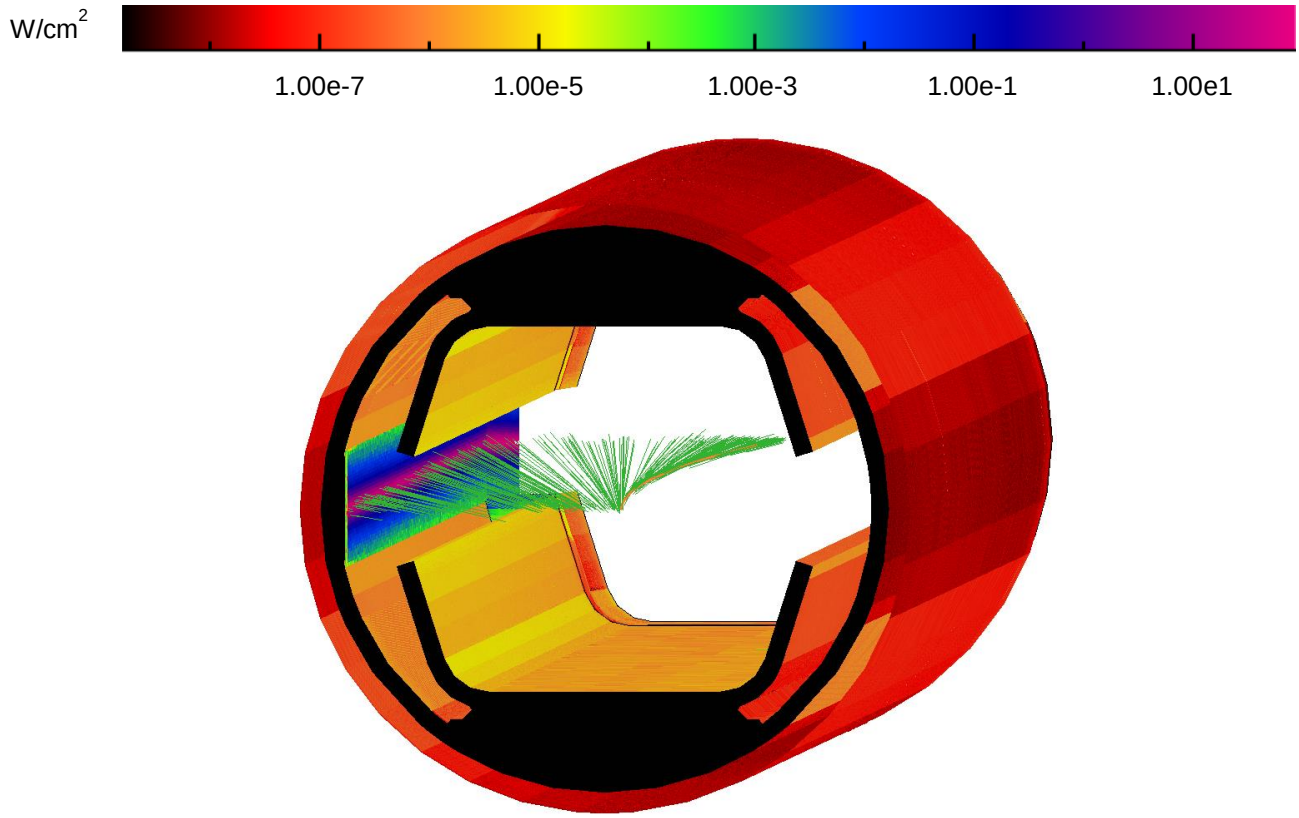

Figure 11. Ray tracing results of the SR power generated by a 50 TeV, 500 mA beam, 15.78 T in a standard arc dipole chamber, as obtained with Synrad+ [13]. The beam sagitta and photon trajectories can be clearly appreciated

Extensive ray photon tracing simulations have been performed to obtain a complete map of the SR inside the vacuum chamber. This has allowed to acquire inputs for the e-cloud studies [14] and for the thermomechanical [6, 7] and coupled vacuum simulations [13]. The results for a simple arc cell dipole (MB) can be found in Figure 11, for 50 TeV, 500 mA, 14.242 m magnetic length, non-ideal beam, 15.78 T magnetic field and ideal sawtooth geometry. The reflectivity of each material has been taken into account for all the performed analysis. Table 3 shows a summary of the SR power distribution in the MB's BS. Most part of the power > 90 % is absorbed on the sawtooth present in the secondary chamber, and it can be seen how the leaked power to the cold mass and inner chamber results to be negligible, due to the low reflectivity of the X-rays.

Figure 12 shows the photon ray tracing (for a previous geometry, with wider SR absorbers) performed in a series of three dipoles, separated by their standard angle, 0.077º, and a SSS, with half of the dipole angle to allow a straight pass of the beam. It can be seen how the SR emitted at the end of each dipole reaches two dipoles downstream, with an average photon path of 21 m. The shadow produced by each absorber can also be noticed. Regarding the SSS, the radiation produced by the quadrupoles (MQ) and other magnets has been found to be negligible compared to the one emitted by the MB, both in flux and in critical energy, so they have been discarded from the analysis.

Table 3. SR power distribution in the arc for 50 TeV, 500 mA ideal sawtooth geometry

Area	**Power**	**Fraction of MB**
Irradiated baffle	449.8 W	91.3 %
End absorber	42.4 W	8.6 %
Inner copper primary chamber	0.09 W	0.02 %
Interconnect	0.07 W	0.01 %
Non-irradiated baffle	0.04 W	0.01 %
Other BS areas	0.01 W	< 0.001 %
Cold bore	0.001 W	< 0.001 %
Total per arc dipole	492.4 W	100 %

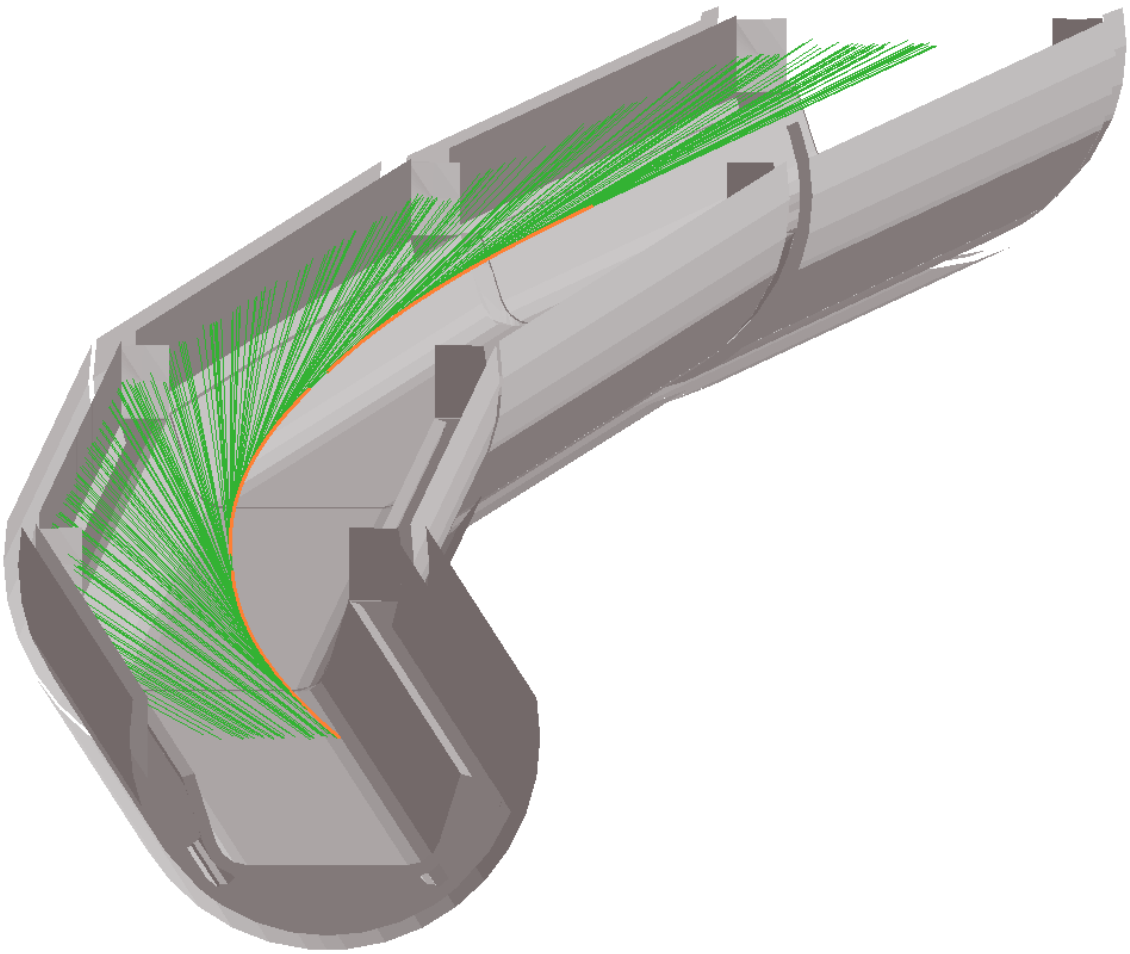

Figure 12. Ray tracing simulation of the SR flux generated by a 50 TeV, 500 mA beam, 15.78 T in the vacuum chamber of three consecutive MQ and a SSS, highlighting in green the photon trajectories

6. BEAM INDUCED EFFECTS

The molecular density of the residual gas in the FCC-hh vacuum chamber can be expressed with the following formula:

$$n_g = \frac{P}{kT} = \frac{Q}{S \cdot kT} = \frac{\overbrace{(\eta_{ph} + \eta'_{ph}) \cdot \dot{\Gamma}_{ph}}^{\textit{photon-induced desorption}} + \overbrace{(\eta_e + \eta'_e) \cdot \varphi_e}^{\text{e-induced desorption}} + \overbrace{\sum(\eta_j + \eta'_j) \cdot \sigma_g \cdot \frac{I}{e} n_g}^{\text{ion-induced desorption}} + \overbrace{A \cdot q_g}^{\text{thermal outgassing}}}{S \cdot kT} \quad (6)$$

Where n_g is the molecular gas density, which as defined in Section 2 has to be < $1 \cdot 10^{15}$ $H_{2\,eq}/m^3$,

P is the pressure,

k the Boltzmann constant,

T is the temperature,

Q is outgassing,

S is the pumping speed, expressed in the same range as the outgassing,

η_{ph} and η'_{ph} are the primary and secondary photon MDY, respectively,

η_e and η'_e are the primary and secondary electron MDY,

$\dot{\Gamma}_{ph}$ is the photon flux on the chamber's wall,

φ_e is the electron impingement rate hitting the chamber's wall,

σ_g is the gas ionization cross section,

η_j and η'_j are the primary and secondary ion MDY,

A is the area, in the same range as Q and S, and q_g the thermal outgassing per area unit.

In all cases, all four main species (H_2, CO, CO_2, CH_4) have been contemplated for all the outgassing sources. The thermal outgassing and vapor pressures are the only sources of outgassing during static mode, without beam, and they are negligible during dynamic mode, when the main beam induced effects surpass its contribution by many orders of magnitude.

We have considered the interior of the beam screen to be at equilibrium during dynamic mode: the increase of desorption derived from the coverage growth is balanced by the effective pumping of the surfaces at 40-60 K. The model can be simplified then, avoiding the use of many unknown parameters as sticking probabilities or recycling yields at cryogenic temperatures. For the cold mass, given the size of the p. holes and the high coverages which can be achieved there, recycling effects have been considered for SR. As a pessimistic estimation, and to better check the feasibility of the vacuum system, no beam pumping nor photo-cracking effects have been contemplated. Taking them into account (when enough literature data were available to model them) would only improve the resulting H_2 equivalent MD. No transient effects caused by the temperature variations have been contemplated either, since they belong to the studies of vacuum stability, i.e. Task 4.4.

It is also important to highlight that most of the inputs necessary to perform the corresponding calculations are missing in the literature, so conservative estimations have been used in most cases.

PHOTON STIMULATED DESORPTION (PSD)

6.1.1. Primary desorption

This phenomenon is the primary gas source in all the existing electron synchrotron light sources. The SR energy releases electrons when the photons hit the vacuum chamber walls, and the electrons in turn make the trapped gas to be released from the surface into the vacuum chamber. MDY values have been studied in the past for a large variety of materials and SR critical energies. Photon MDY values are placed typically in the range of 10^{-3} - 10^{-5} molecules per photon. These values are proportional to the gas content and they decrease along with the photon dose that the surface receives, with a typically decaying rate after an initial plateau following the expression [15]:

$$\eta = \eta_0 \cdot D^{-a} \tag{7}$$

Where η is the yield in molecules/photon depending on the dose,
η_0 is the initial yield,
D is the integrated photon dose, usually expressed in ph/m in the literature,
a is the decaying slope (in log-log scale), with values between 0.6-1.

Extensive MDY studies were carried out for the LHC conditions, as well [16]. Nevertheless, for the FCC-hh BS values (4238 eV ε_c, 40-80 K unbaked Cu) no experiment has ever been done, owing to the exceptionally high energy the FCC-hh would have: except for the FCC-hh, all the proton accelerators generate very low critical energies (< 50 eV) and the electron accelerators, with much higher critical energies, do not need superconducting magnets and cryogenic temperatures.
Therefore, in order to calculate the pressure contribution of the PSD, estimations of the photon MDY values have been done for the FCC-hh conditions, in order to use them later in the corresponding molecular density calculations. Due to the intrinsic uncertainty of these estimations, and in order to guarantee a good performance prediction of the FCC-hh vacuum system, the MDY values shall be experimentally acquired in the future.
As studied in the past, for a defined material, the MDY is lower the lower the temperature is [17] (the gas molecules need a higher amount of transferred energy to be released) and higher the higher the critical energy is [18] with a noticeable tendency (see Figure 13b). The slope a can be also plotted against ε_c, with a very good curve fitting. All these known proportions and curves have been then used to scale the estimations to the FCC-hh conditions. The resulting curves, for stainless steel (SS) and copper, are plotted in Figure 13a. Both curves result to be similar, higher than LHC data as expected, and lower than the same materials at room temperature (RT). The shown data take already into account all common gas species, expressed in *hydrogen equivalent* yield according to Equation 8 and using values from Table 4. The high reduction in the equivalent MDY from RT to 77 K is mainly explained by the high reduction in the CO and CO_2 yield [17], being them the species with the highest relative impact in the nuclear scattering beam lifetime.

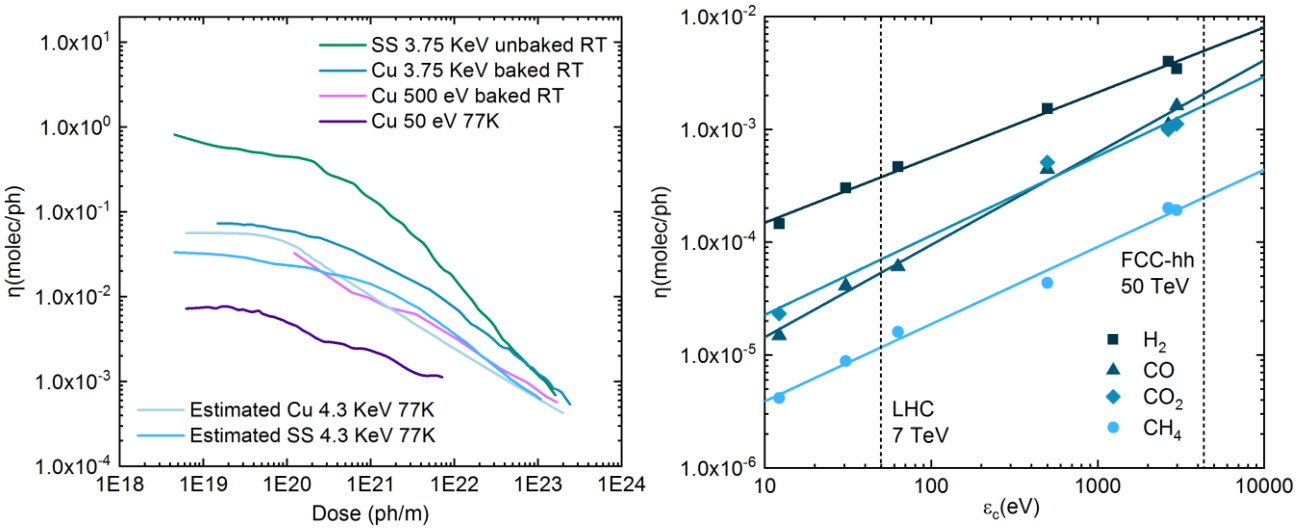

(a) H_2 equivalent molecular yield for various materials, temperatures and energies [35, 34, 36, 16]

(b) MDY dependence on ε_c for the common gas species of baked Cu at RT [18, 33]

Figure 13. Comparison of the different H_2 equivalent molecular yield for different materials and conditions, including the estimated ones for the FCC-hh. An evolution of the yield vs critical energy is also shown on the right side

$$\eta_{H_2 eq} = \sum \eta_g \cdot \sigma_{g\,H_2 rel} \cdot S_{g\,H_2 rel} \tag{8}$$

$$S_{g\,H_2 rel} \approx \sqrt{M_g / M_{H_2}} \tag{9}$$

Where $\sigma_{g\,H_2 rel}$ is the relative cross section, used in Equation 1,

$S_{g\,H_2 rel}$ is the relative conductance/p. speed, approximated with Equation 9,

and M is the gas molar mass.

Table 4. Proportionality to H_2 of common gas species

Gas species	**Cross section relative index** [19]	**Conductance relative index**	**Total H_2 equivalent index**
H_2	1	1	1
CO	9	3.7	33.5
CO_2	13.9	4.7	64.9
CH4	6	2.8	16.8

Knowing the MDY for each species and dose, and with the flux per area found with the photon ray tracing shown in Section 5, it is possible to calculate the resulting molecular density due to the PSD for any time with the corresponding terms of Equation 6. Results are displayed in Section 7.

6.1.2. Secondary desorption (recycling effect)

The secondary photon stimulated desorption is the increase of the desorption yield owing to the condensed gas layers being released at lower and lower energies as the thickness of the layer increases. As previously stated, this effect is not taken into account inside the beam screen considering that the high radiation flux present is continuously cleaning the surface and setting the coverage in an equilibrium state, compensated by the sticking factor that the surface presents.

Secondary desorption has been only taken into account for the case of the cold bore, where all the desorbed gas from inside the BS is accumulated over time and the leaked radiation through the pumping holes can trigger its secondary desorption. The coverage can then grow up to considerably high levels, yielding an increase of MDY of several orders of magnitude higher than a bare surface just within the first days of vacuum conditioning. The MDY values for a wide range of coverages can be found in Figure 14:

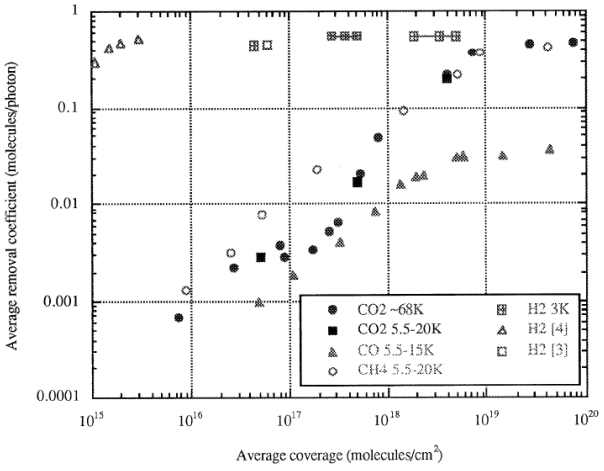

Figure 14. Secondary photon molecular desorption yield of common gas species vs surface coverage [20]. Equivalent ε_c after slits is around 290 eV

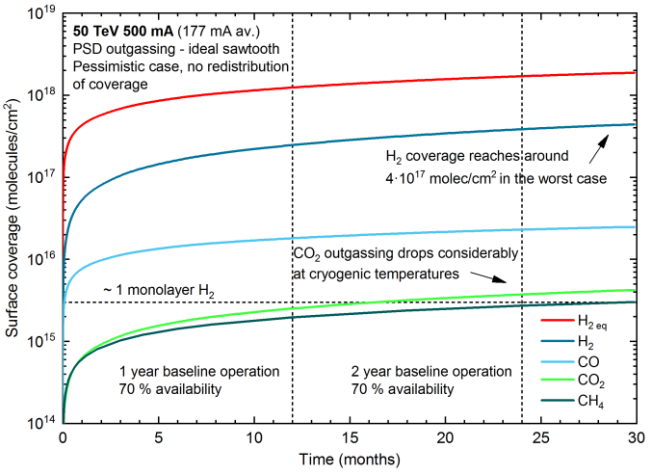

Figure 15. Coverage evolution of different gas species over time coming from PSD, for an ideal sawtooth geometry and 70% machine availability

It is shown how H_2 has a high recycling rate, whilst the other gases require thicker coverages to have a non-relevant yield. As a pessimistic case, the coverage has been calculated integrating the total desorbed molecules from PSD (rounding it up as 100% of the total outgassing, as an estimation) and distributing uniformly their amount in the cold bore area directly facing the pumping holes apertures, as shown in Figure 3, obtaining then numbers of molecules/cm^2. This coverage can be plotted over time, as seen in Figure 15. In reality, the coverage is expected to be distributed over the cold bore although in a non-uniform way. The yields for low coverages have been extrapolated, since they are not available in the literature.

One critical point to highlight is the role of the critical energy in the secondary desorption. Even if it has not been studied, the MDY dependence on photon energy is expected to be similar to the primary desorption (see Figure 13b). As such, the spectrum of the leaked SR would have to be considered in this kind of calculations. Besides, the shown data were acquired for temperatures higher than the one

the cold bore will have (1.9 K) which is expected to slightly decrease the MDY. Finally, owing to the lack of data, and with the idea of the feasibility study in mind, pessimistic yields available in the literature [20] have been then directly used, even if the ε_c of the documented experiment (around 290 eV) is much higher than the ε_c of the SR arriving to the cold bore (< 10 eV, as seen in Figure 17), using ε_c as the original definition of the energy dividing the power spectrum expressed in 0.1% BW in two equal halves.

With the data obtained in the ray tracing procedure and knowing the yield at each time, it is straightforward to estimate the resulting molecular density due to this effect (Equation 6). Results over time are shown in Figure 16. Since H_2 is the molecule with highest MDY, it is expected to be the predominant molecule of the gas composition due to the secondary desorption. And since the MDY seems to be constant once reached the monolayer (around $3 \cdot 10^{15}$) for this species, the pressure contribution of this effect can be considered constant from the first week until the second year of operation, low enough to avoid the total pressure exceed the established requirement of $1 \cdot 10^{15}$ $H_{2\,eq}/m^3$. A 70% machine availability and 1 month of stop per year have been taken into account in this calculation.

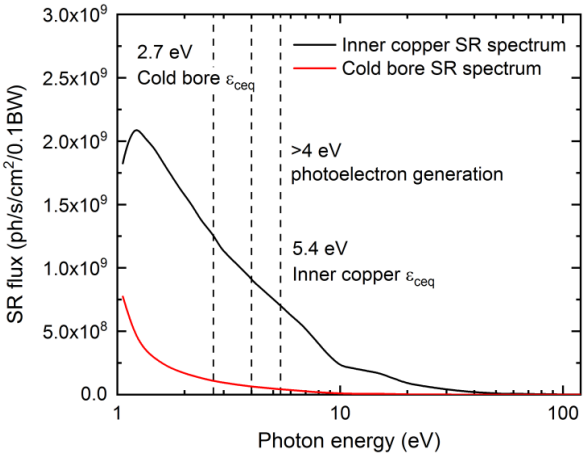

Figure 17. Spectrum of the SR reaching the cold mass and the inner chamber, for a 50 TeV and 500 mA beam. Ideal sawtooth geometry

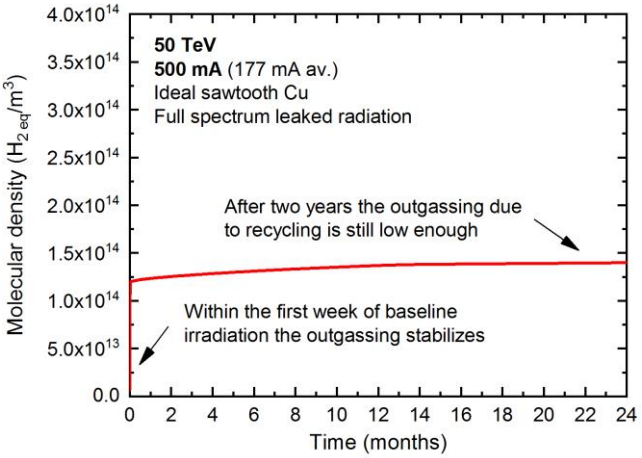

Figure 16. MD contribution of recycling effect over time, with full spectrum flux and ideal sawtooth

Dedicated experiments to measure the secondary molecular desorption yield for the conditions of the FCC-hh, and/or density measurements of a prototype at cryogenic temperatures are mandatory to properly characterize and model the recycling effect in the vacuum chamber of the new collider.

ELECTRON STIMULATED DESORPTION (ESD)

As its name indicates, ESD happens when the electrons hitting the vacuum chamber's walls transmit part of their energy to the gas molecules on the material's surface and release them into the system, rising then the residual gas molecular density.

The impinging electrons are part of the e-cloud, which as it is known is originated by the periodic passage of the beam and its attractive interaction with the electrons generated in the chamber either by SR or by proton beam ionization of the residual gas molecules. Since the average amount of molecules released per impinging electron is known, as is the electron flux/impingement rate, the outgassing and thus the pressure contribution from this effect can be found (see Equation 10 [21]).

The electron cloud density and thus the electron impingement rate, φ_e, is proportional and very dependent on the rate of photoelectrons generation, N_e, as shown in Equation 11 and in Figure 18. A variation of just a 30% within the values close to unity can yield changes of three orders of magnitude.

The primary source of electrons which are accelerated and form the e-cloud is, in turn, the photoelectrons generated thanks to the photoelectric effect, when the SR flux ($\dot{\Gamma}_{ph}$) hits the chamber walls. This is represented in Equation 12, which takes into account the photon flux spectrum and the photoelectron yield (Y_{ph}) depending on the photon energy.

As such, and since the ESD outgassing is proportional to the SR flux and power reaching the areas were the e-cloud build-up happens, this is why reducing the amount of SR reaching these areas is of the utmost importance. As previously stated, the sawtooth finishing and the double chamber structure help to minimize the SR scattering to these areas.

$$\Delta P_{ESD} = kT \frac{\int_{E_{min}}^{E_{max}} \eta_e(E)\, \varphi_e(E)}{S} \tag{10}$$

$$\varphi_e(E) \propto N_e \tag{11}$$

$$N_e = \int_{E_{min}}^{E_{max}} \dot{\Gamma}_{ph}(E)\, Y_{ph}(E) \tag{12}$$

Where ΔP_{ESD} is the variation of pressure due to ESD,

η_e is the molecular desorption yield (MDY) per electron,

φ_e is the electron impingement rate hitting the chamber's wall,

N_e is the electron generation rate on the chamber's surface,

$\dot{\Gamma}_{ph}$ is the photon flux hitting the chamber's surface,

Y_{ph} is the photoelectron yield, depending on the photon energy.

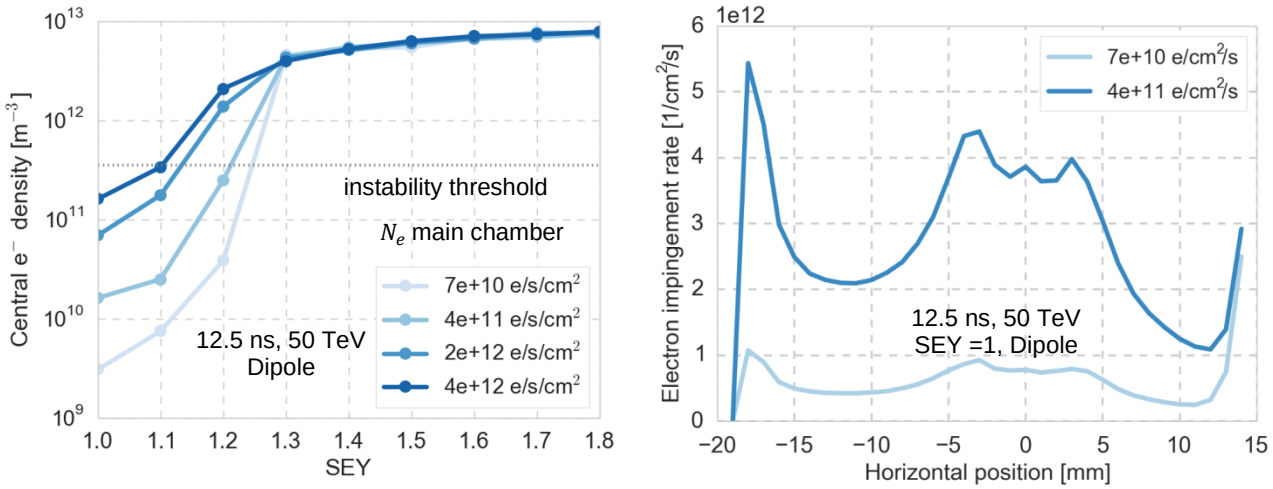

(a) e- density vs SEY *(b) Impingement vs horizontal position*

Figure 18. Preliminary electron density and impingement rates depending on photoelectron generation rate and SEY, in a dipole chamber with 12.5 ns 50 TeV beam, as an example. Courtesy of L. Mether, EuroCirCol WP2 [22]

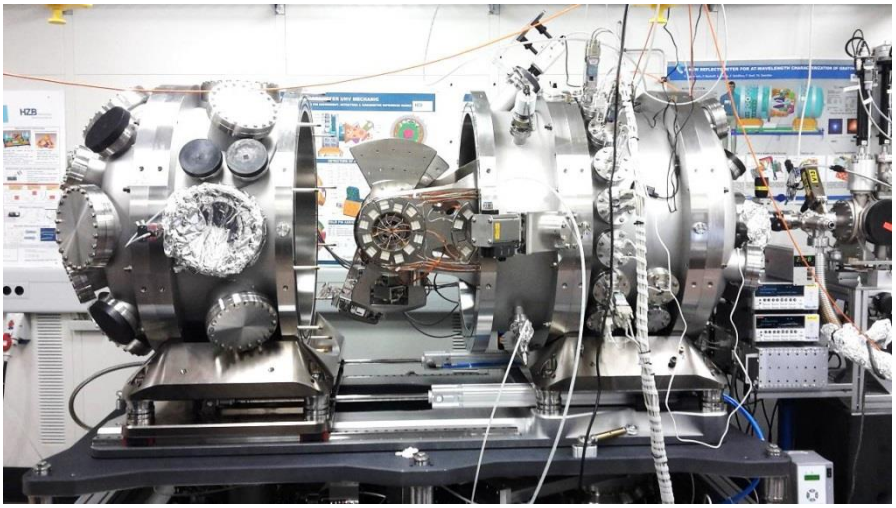

Figure 19. Reflectometer in BESSY II's beamline [23], showing part of the rotating system to align samples

The photoelectron yield, Y_{ph}, is characteristic of each material and it not only depends on the incident photon energy but also on the incident angle [24]. Photoelectrons are only produced above the material's work function, around 4.7 eV for Cu. Being the photoelectron yield and reflectivity unknown for LASE (the chosen solution to mitigate SEY), and owing to its importance, a dedicated experimental plan was arranged to obtain the missing data. In a collaboration led by LNF-INFN, baseline LASE [12] and an LHC's Cu BS were measured, among other materials, in a dedicated beamline at the BESSY II light source [23], Germany. Figure 19 shows the reflectometer used to

measure the Y_{ph} and the reflectivity of the positioned sample. Measurements are carried out with the possibility of changing the incident SR energy from 35 eV to 1800 eV and also the impact angle. The scattered light is collected with a GaAsP photodiode, which can also vary its position obtaining lectures of scattered light at different angles. The photoelectron yield is obtained with the lectures of the drained current in the sample and with the direct beam photon flux measurement. For LASE Cu, the photoelectron yield and reflectivity have been found to be substantially lower than for untreated copper, as it was expected, yielding very low electron densities and impingement rates on the vacuum chamber. Together with its low SEY, the reduction of these properties is explained by its high aspect ratio (see Figure 7). Measured data are expected to be published in the future [25]. With these data and with the output from Synrad+ Monte Carlo simulations the electron generation rate, N_e, has been found and sent to the EuroCirCol's WP2 to run the corresponding electron cloud simulations. The generated inputs were received by the WP4 and used to calculate the ESD contribution to the total pressure. Results are shown in Section 7. As expected, owing to the good properties of the mitigation treatment and the low SR scattering, the molecular density present in the vacuum chamber coming from ESD is kept within the specifications. Besides of the associated electron impingement rate, results obtained by the WP2 show that the SR flux reaching the build-up areas is low enough to keep the electron density below the instability threshold, providing the SEY is below the established limits [14]. Thanks to the electron density maps, it is also possible to know the critical areas where the e-cloud is developed, and thus the BS surface to treat, as depicted in Figure 21:

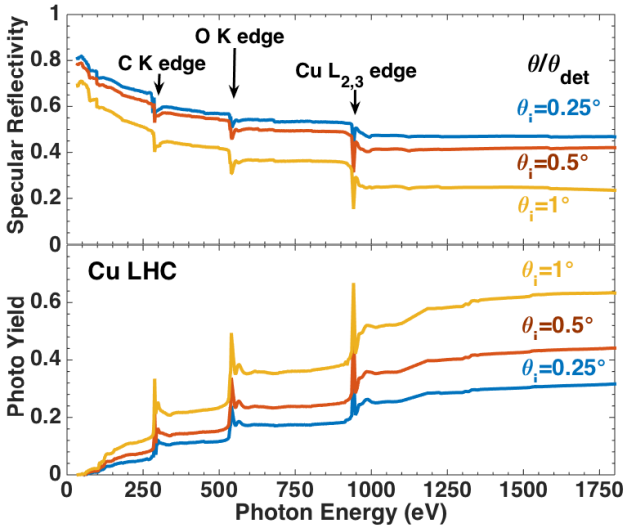

Figure 20. Example of Y_{ph} vs energy, as obtained in BESSY II's experimental run [37]

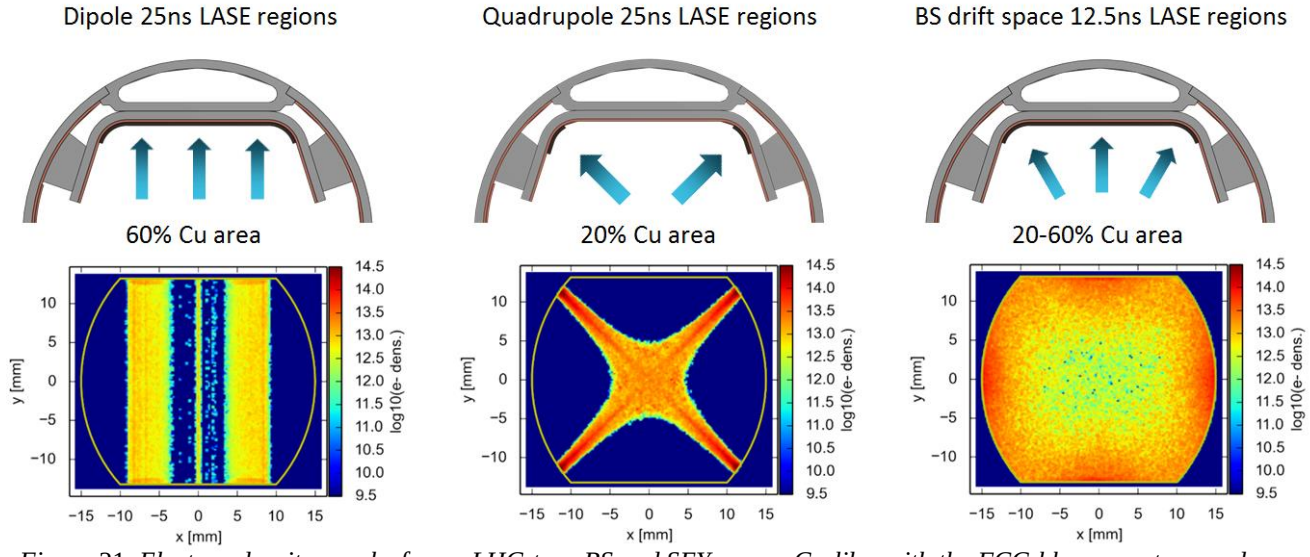

Figure 21. Electron density graphs for an LHC-type BS and SEY curves Cu-like, with the FCC-hh parameters, and associated areas in a previous FCC-hh BS geometry. Courtesy of L. Mether, EuroCirCol WP2 [22]

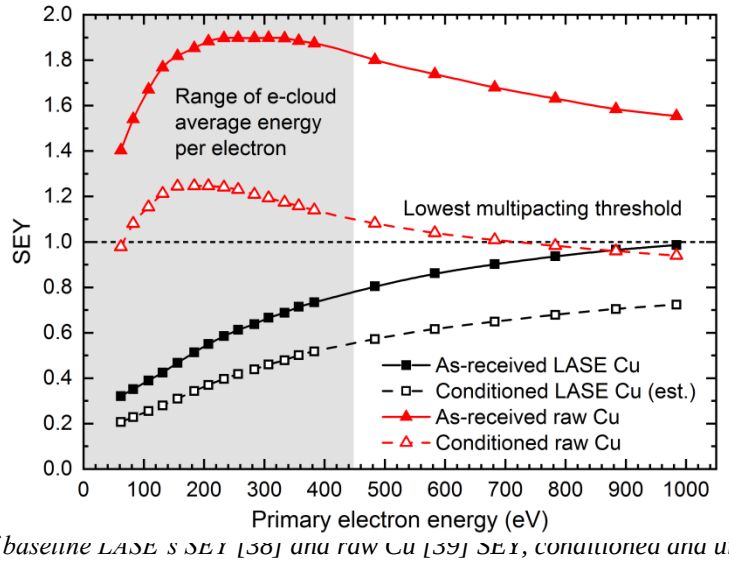

Figure 22. Comparison of baseline LASE's SEY [38] and raw Cu [39] SEY, conditioned and unconditioned. The range of most common electron energies is also shown for SEY curves Cu-like [40]

Running a pessimistic case, absorption rate has been set as total in the ray tracing simulations for LASE. Even if at low photon energies it presents some reflectivity, those photons are not sufficient to contribute significantly to the total amount of generated electrons per second N_e. Figure 20 shows an example of the decaying tendency of Y_{ph} vs energy. High energy photons are the ones yielding a significant photoelectron yield. Besides, owing to the reflectivity dependence on energy, as depicted in Figure 6, for an ideal sawtooth geometry only low energy photons would reach the inner chamber. For the case of LASE, this dependence is similar.

For the sake of completeness, SEY of LASE is also shown in Figure 22. It can be compared with the latest SEY requirements of the FCC-hh shown in Table 5. Except for the 12.5 ns option, LASE would not be strictly mandatory for dipoles, which constitute more than 80 % of the arcs length, and the requirements could be potentially achieved with beam scrubbing. Also important to mention is the fact that the properties of LASE treatment can be adjusted. Decreasing the deposition of energy on the surface during the laser ablation reduces the aspect ratio and the impedance of the final product, increasing in turn the SEY and Y_{ph}. To minimize the impedance, then, the margin between the requirements and the material's value for each region should be as narrow as possible. With regard to the electron MDY used in the calculations, Cu estimations already present in the literature have been used for the time being [26], owing to the lack of experimental data. Experiments to measure these values are expected to be performed in the future within EuroCirCol's framework.

Table 5. Summary of the latest SEY requirements, for different arc regions, bunch spacing, and energies (injection/baseline) for SEY curves Cu-like. Courtesy of L. Mether, EuroCirCol WP2 [14]

Bunch spacing	**25 ns**		**12 .5 ns**		**5 ns**	
E [TeV]	**3.3**	**50**	**3.3**	**50**	**3.3**	**50**
Dipole	1.4	1.4	1.1	1.1	1.5	1.5
Quadrupole	1.1	1.2	1.0	1.0	1.1	1.0
Drift space	2.0	2.0	1.3	1.3	1.6	1.6

ION STIMULATED DESORPTION (ISD)

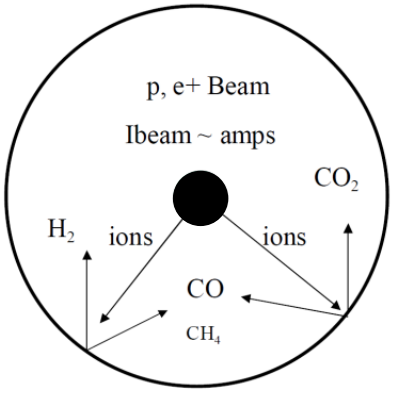

Figure 23. Representation of the ISD mechanism [15]

The positively charged proton beam in the FCC-hh can ionize residual gas molecules in its path. The created ions are repelled by the positive space-charge potential and are accelerated towards the vacuum chamber walls, with an energy of several hundred eV per ampere of circulating current. The high energy the ions can achieve makes them very effective in desorbing strongly-bound gas molecules. Being the rate of ionization proportional to the residual gas density, an avalanche process may then occur resulting in a continuously increasing pressure [15], triggering a pressure overrun and exceeding the molecular density limit.

For low beam currents, and since the pressure increase is proportional to its value, the additional outgassing owing to the ion creation is compensated with the pumping system, keeping the pressure higher but in equilibrium. However, for currents higher than a critical value, no equilibrium value exists (see Equation 13). The vacuum system shall be therefore designed to keep the critical current (I_c, Equation 14) far enough from the baseline current values, mainly by means of a sufficiently high pumping speed. A factor of two difference is recommended [27].

The total ion MDY η_j can be separated in a primary and a secondary (recycling) component, at the same time. Nevertheless, as the case of the η_e, this yield is usually neglected as the surface coverage inside the beam screen is considered to be in equilibrium and low.

$$P(I) = \frac{P_0}{1 - I \cdot \frac{\sigma_g}{e} \cdot \frac{(\eta_j + \eta'_j)}{S}} \tag{13}$$

$$I_c = \frac{e \cdot S}{\sigma_g \cdot (\eta_j + \eta'_j)} \tag{14}$$

Where $P(I)$ is the corrected, resulting pressure,

P_0 is the initial pressure,

S is the pumping speed in the analyzed area,

I_c is the critical current,

I the analyzed beam current, generally the maximum one,

σ_g is the gas ionization cross section (see Table 6),

η_j is the primary ion MDY,

η'_j is the secondary ion MDY.

As a fast estimation of the pressure contribution of this effect, a single gas model has been chosen for the time being. If the difference between I_c and I is high enough, the ISD outgassing should be negligible compared with the other beam induced effects. Since I_c depends directly on the pumping speed S, it is easy to determine that the regions with the lowest I_c are the interconnections, due to the absence of direct cryopumping and the low conductance the small diameter of the BS grants.
It is also known that the most dangerous species is usually CO due to its relative high ionization cross section, high MDY and low pumping speed, being also the gas with the highest contribution in the beam lifetime. For this reason, and for the single gas model, a RT molecular mass = 18 unconditioned MDY present in the literature has been chosen [28]. With regard to the ionization cross section, new values corresponding to the higher energy of the FCC-hh have been estimated (see Table 6). The pumping speed in the most central area of interconnect has been also calculated for each gas, for a conservative temperature of 40 K. Pessimistic sticking coefficients have been also taken into account for CO, CO_2 and CH_4 [29], for the non-irradiated areas of the bellows, even if they are not affecting to any great extent to the final pumping speed.
Final values of the calculated value for I_c and related pressure increase are displayed in Table 7. I_c values are found to be well above the baseline beam current. Values for inside the magnets have found to be > 50 A, with related pressure increases of < 1%, due to the high pumping speed present.

Therefore, ISD is not expected to be a problem in the arcs of the FCC-hh if the separation between cryostats in the FCC-hh is the same as the one present in the LHC.
This effect would then deliver a minor pressure increase compared with the other beam induced effects. It has to be taken into account, however, in the final design of the magnets interconnection, in order to guarantee a pumping speed high enough to be able to keep a good ratio I_c/I.

Table 6. Comparison of the ionization cross sections for the FCC-hh and previous proton accelerators, with a clear dependence on the energy [41]

Beam ionization cross section (σ_g) 10^{-22} m^2			
Gas/Beam energy	**0.45 TeV (SPS)**	**7 TeV (LHC)**	**50 TeV (FCC-hh)**
H2	0.36	0.45	0.51
CO	2.2	2.7	3.3
CO2	3.4	4.3	5.1
CH4	2.5	3.2	3.7

Table 7. Results of I_c and related pressure increment for the central part of the MB-MB FCC-hh interconnection. Single gas model

Gas/Beam energy	**H_2**	**CO**	**CO_2**	**CH_4**
I_c	29 A	4 A	5 A	34 A
Pressure increase	2 %	15 %	11 %	2 %

7. MOLECULAR DENSITY PROFILE IN THE ARCS

The resulting molecular density in the arcs is finally found adding the contributions of all the previously mentioned effects, as shown in Equation 6 (shown here again for the sake of clarity):

$$n_g = \frac{P}{kT} = \frac{Q}{S \cdot kT} = \frac{\overbrace{(\eta_{ph} + \eta'_{ph}) \cdot \dot{\Gamma}_{ph}}^{\textit{photon-induced desorption}} + \overbrace{(\eta_e + \eta'_e) \cdot \varphi_e}^{\text{e-induced desorption}} + \overbrace{\sum(\eta_j + \eta'_j) \cdot \sigma_g \cdot \frac{I}{e} n_g}^{\text{ion-induced desorption}} + \overbrace{A \cdot q_g}^{\text{thermal outgassing}}}{S \cdot kT} \quad (6)$$

As the calculations are carried out using all four most common gas species (H_2, CO, CO_2, CH_4) we can get an estimation of the particular and global gas composition, as shown in Figure 24. However, the real composition is expected to give H_2 a smaller percentage, since the recycling effect, which is mostly H_2, has been calculated in a conservative way due to the lack of experimental data.

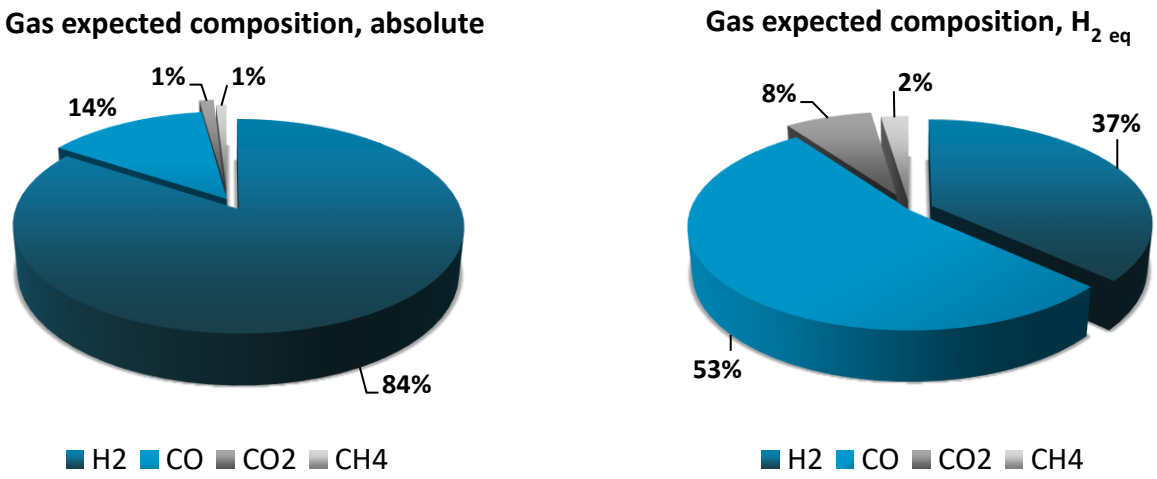

Figure 24. Expected gas composition in the MB, expressed in absolute values and in $H_{2\,eq}$, multiplying each gas by its relative cross section (displayed in Table 4)

The H_2 primary PSD MD profile for a representative arc cell length is shown in Figure 25, using a previous geometry with a bigger photon absorber. The lengths of the MB and SSS are also shown. The pressure bumps in the interconnects can be clearly seen. Figure 26 shows the MD profile with all the calculated beam induced effects for the MB with highest pressure, for the current geometry, with a smaller bump in the interconnect.

For an integrated beam dose of 36 A·h, these preliminary estimations show that the total MD would be below the specifications with enough safety margin. This dose is equivalent to less than 9 days of baseline conditions and a few months of beam current ramping conditioning, limiting the beam energy and current.

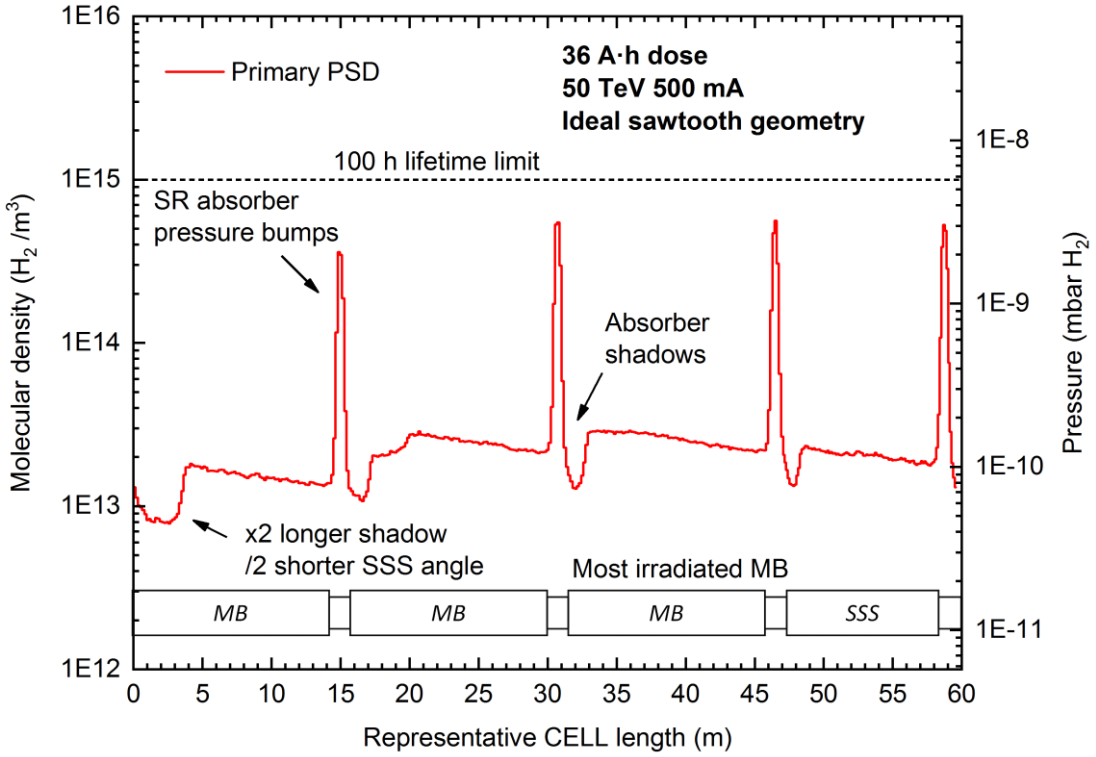

Figure 25. H_2 (non-equivalent) primary PSD MD profile along a representative arc cell length for 50 TeV, 500 mA, 36 A·h. Simulation performed for a previous geometry (Figure 12) with SR absorbers intercepting twice the current power

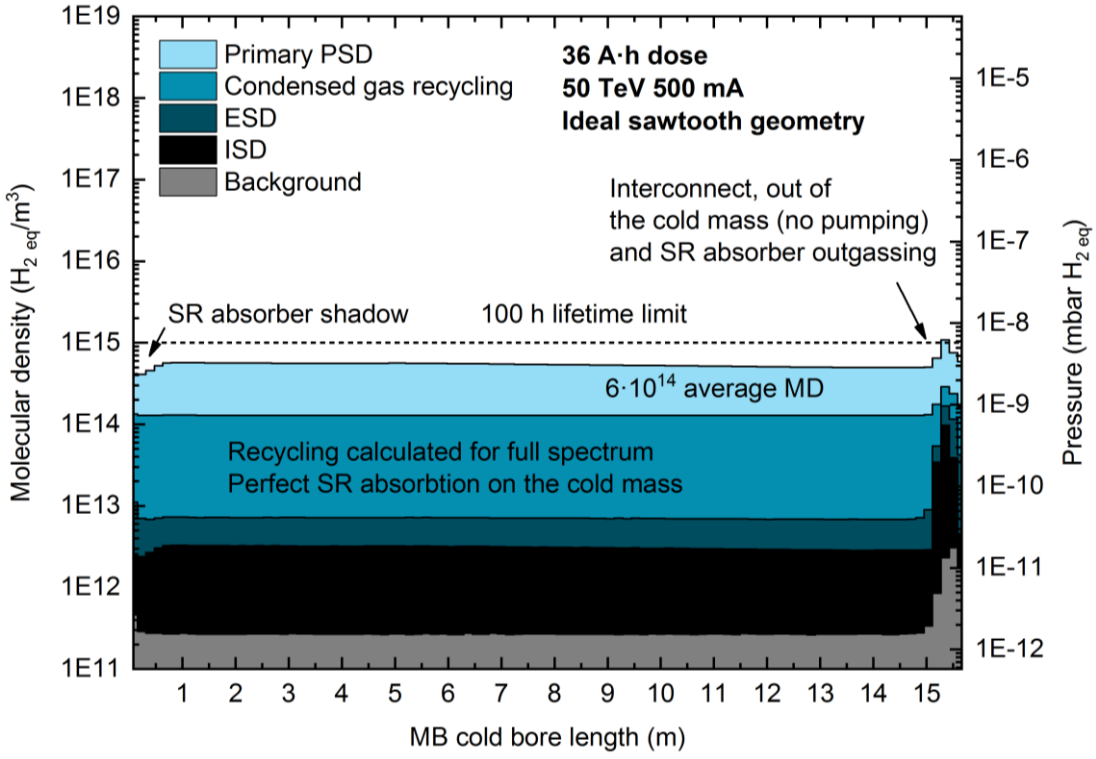

Figure 26. Molecular density profile in the most irradiated FCC-hh MB, for 50 TeV, 500 mA, 36 A·h ideal sawtooth geometry and preliminary ESD data showing the estimated contribution of each beam induced effect

8. EXPECTED HEAT LOAD ON THE COLD MASS

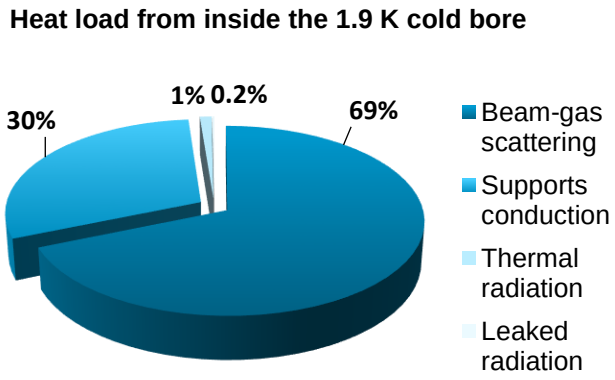

Heat source	Value
Nuclear scattering	191 mW/m
Conduction through supports	83.2 mW/m
Thermal radiation	3 mW/m
Leaked SR power	0.5 mW/m
Total	277.7 mW/m

Figure 27. Distribution of the heat loads to the cold mass coming from the beam screen

The magnets' cold mass is cooled down up to 1.9 K to achieve superconducting properties, with a current density high enough to obtain the required 15.78 T magnetic field. To keep this temperature constant, the liquid He cryoplants deliver the necessary cooling power to counter the different heat loads to which it is subject. 0.3 W/m/aperture [2] are allocated in the heat load budget to the heat coming from inside the cold bore, which in total is 40% of the total thermal budget per magnet.

With the present design, and for the maximum molecular density and baseline parameters, the maximum leaked power emitted from the beam screen towards the inner area of the cold bore is kept below the budget, although with little margin (see Figure 27 for details). More information can be found in [7].
The nuclear scattering has been calculated for a 100 h lifetime (see Equation 2). The beam conditioning is thus expected to decrease this heat source over time as the pressure drops. Besides, the average heat load over time will be somewhat lower than the maximum values shown above due to the current and beam screen temperature decay during runs.

9. KARA LIGHT SOURCE EXPERIMENT, LEARNINGS SO FAR

In the framework of the collaboration, the fabrication of three FCC-hh beam screen prototypes has been carried out with the aim of testing them at RT on the Karlsruhe Institute of Technology (KIT) 2.5 GeV electron storage ring KARA (KArlsruhe Research Accelerator) light source. The prototypes are being tested in a dedicated beamline designed and installed by the collaboration (see Figures 30, 31 and 32), named BESTEX (BEam Screen TEstbench EXperiment). KARA was chosen because of the similarities of its SR spectrum, linear photon flux and power densities, with the ones foreseen for the FCC-hh. For the time being, the first two prototypes have been tested. Results have been recently presented at several international conferences [30, 31]. Preliminary results and the set-up descrtiption were also described in a previous WP4 Deliverable [32]. Up to know, we can extract a series of initial conclusions useful for the design of the FCC-hh vacuum system:

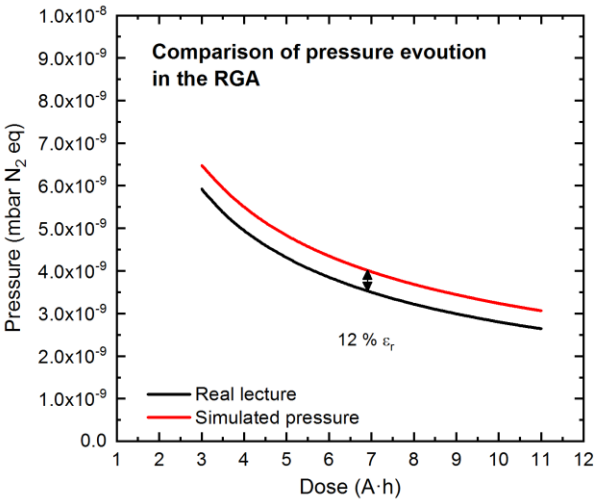

Figure 28. Comparison of the experimental and simulated pressure evolution in BESTEX's RGA

- The theoretical SR scattering caused by a rounded reflector has been experimentally detected, reinforcing the viability of the latest beam screen geometry. Previous BS designs included one sharp tip aiming at redirecting the radiation out of the inner chamber. Nevertheless, the manufacturing process always leaves a small rounded profile on the edge that could scatter the radiation back to the central chamber, increasing the e-cloud density and increasing the pressure due to PSD effect.

- The experimental results are in good agreement with the calculated pressures and photon scattering. In Table 8, and in Figure 28 a comparison of the experimental pressures and the calculated ones is shown, with discrepancies always under 30% for the 1st prototype. Figure 29 displays the experimental readings of dynamic pressure for the 2 first prototypes. For the time being these results contribute to the validation of the theoretical model in a positive way, since the model and computer code developed to predict the molecular density level in the FCC-hh and its evolution over time is the same as the one used for BESTEX. Measurements for the 3rd prototype, the one closest to the current BS geometry, will provide further validation.

- Power deposition calculations, and their related temperature estimations have been experimentally checked in the experiment by the use of PT-100 temperature sensors. Their good match gives good confidence in the photon ray tracing simulations too [31].

- The manufacturing of the prototypes has provided useful inputs for the BS design for 2 x 100 km rings [6, 7].
- In a vacuum system, the influence of photon scattering increases the theoretical outgassing according to the total received dose. As previously stated, this has been one of the main reasons to choose the sawtooth surface finishing as a scattering mitigation solution. Testing the 3rd prototype will provide useful data to check the pressure reduction due to this effect, when compared with the 1st and 2nd prototypes.

Future work will also provide data with regard to the LASE dynamic outgassing and sawtooth reflectivity. Final measurements are expected to be carried out by the end of the year.

Table 8. Comparison of the experimental pressure readings and the calculations at BESTEX experiment, for the first prototype

Dose	**3.12Ah**		**9.36 Ah**	
Lecture	Experiment	Calculations	Experiment	Calculations
Middle (mbar)	5.8E-9	6.3E-9	2.9E-9	3.4E-9
Front (mbar)	3.0E-9	3.0E-9	1.9E-9	1.7E-9
Back (mbar)	2.0E-9	2.8E-9	1.1E-9	1.5E-9

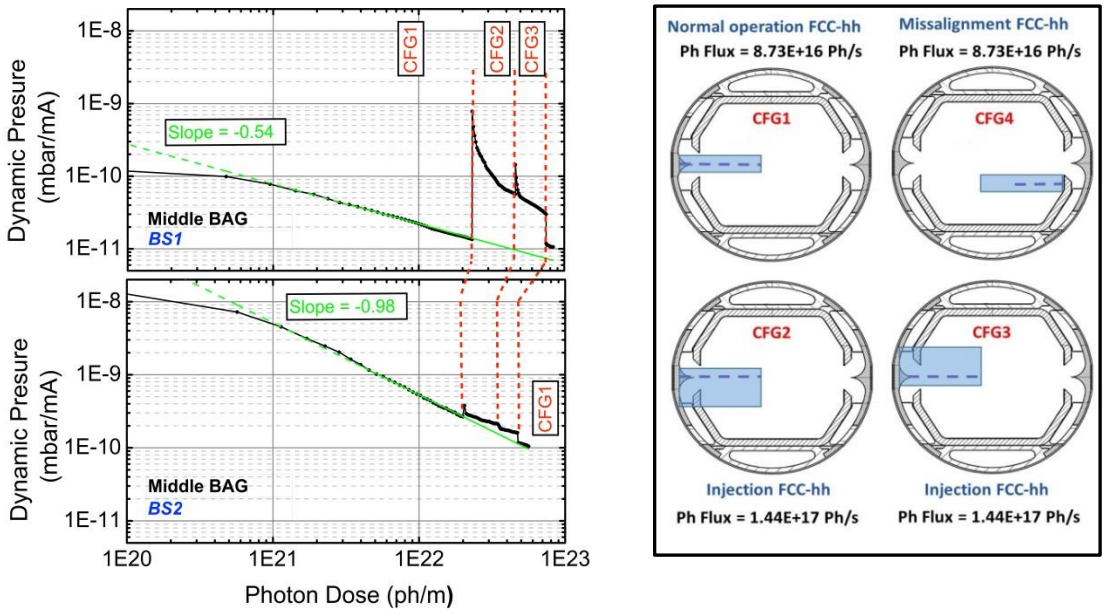

Figure 29. Readings of dynamic pressure evolution and irradiation configurations at BESTEX, for the 1st and 2nd prototypes, as shown in [30]

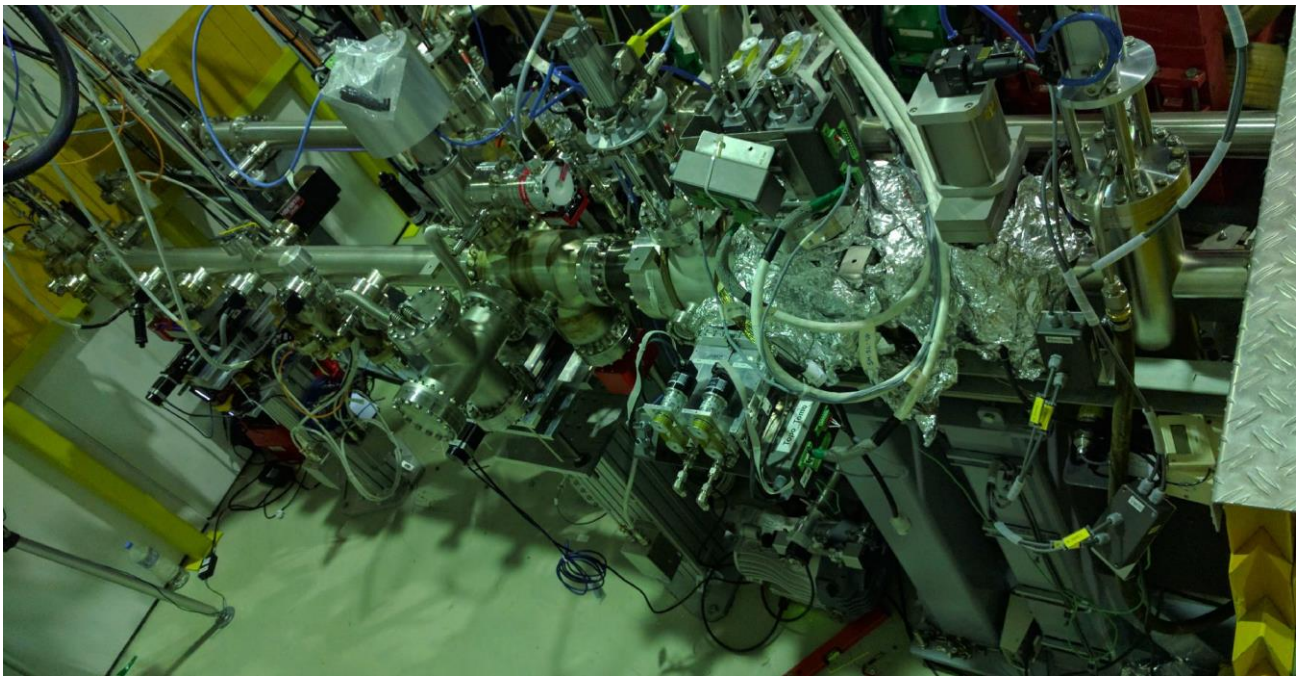

Figure 30. Complete BESTEX set-up at the KARA light source, already commissioned

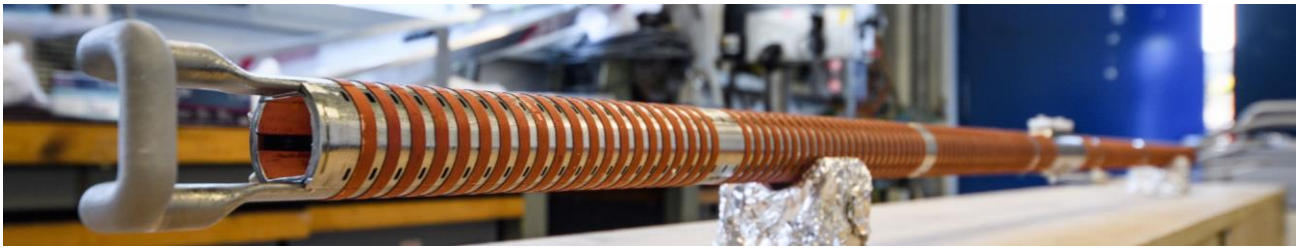

Figure 31. First BS prototype tested in BESTEX, before being inserted in the vacuum chamber

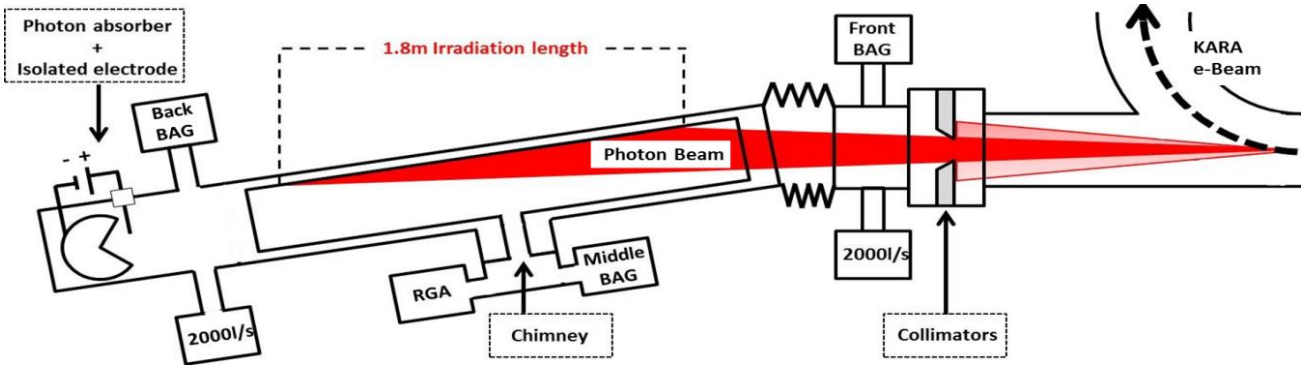

Figure 32. Schematic representation of the BESTEX experiment [30], showing the different points of pressure reading

10. CONCLUSIONS AND FUTURE WORK SUGGESTIONS

- The preliminary results discussed so far suggest that the concept of the vacuum system of the FCC-hh based on a novel BS design should work. The molecular density in the arcs of the FCC-hh shall be sufficiently low, with a reasonably short conditioning time of a few months, similar to that of the LHC. No critical showstopper has been identified up to now.

- CO seems to be the most impacting gas species on the beam lifetime, while H_2 is the most common, as expected.

- The proposed SEY mitigation solution, LASE, would reduce considerably the ESD pressure contribution, for an ideal sawtooth geometry. LASE parameters could be adjusted to meet the specifications with a narrower margin and thus improve its impedance properties.

- The BESTEX experiment is advancing well and providing good hints to validate the computer tools used to carry out the vacuum simulations for the FCC-hh.

- Due to the high uncertainty of the performed estimations, an extensive experimental plan is required to completely validate the analysis of the beam induced vacuum effects and the efficacy of the proposed mitigation measures. Tests of the prototype at cryogenic temperature and with the FCC-hh SR features shall be performed to measure the photon MDY and the recycling contribution to the total MD in the vacuum chamber. Electron MDY is also mandatory to be measured for the latest SEY mitigation measure chosen and in cryogenic conditions.

- Further simulations with a more realistic sawtooth surface geometry are on-going. The deviations of the real manufactured product from the ideal geometry are expected to increase the outgassing due to PSD and the amount of generated photoelectrons in the vacuum chamber, increasing consequently the ESD outgassing and total pressure. Deviations of the real reflectivity from theoretical one have been already observed experimentally at BESSY II. Extensive studies to adapt the LHC sawtooth geometry to cope with the FCC-hh conditions will also have to be carried out in the future.

11. REFERENCES

[1] "Beam Lifetime, Taking a closer look at LHC," April 2018. [Online]. Available: https://www.lhc-closer.es/taking_a_closer_look_at_lhc/0.beam_lifetime.

[2] C. Kotnig, *Cold mass cooling with supercritical helium,* 2nd FCC Cryogenics Day, Dresden, 2016.

[3] A. Infantino, *private comunnication,* Geneva, Switzerland: CERN, 2017.

[4] A. Infantino, *FLUKA Monte Carlo modelling of the FCC arc cell: radiation environment and energy deposition due to beam-gas interaction,* FCC Week 2017, Berlin.

[5] P. Lebrun and L. Tavian, "Beyond the Large Hadron Collider: a first look at cryogenics for CERN Future Circular Colliders," *Physics Procedia,* vol. 67, pp. 768 - 775, 2015.

[6] F. Pérez, P. Chiggiato, C. Garion and J. Fernández, "Preliminary beam screen and beam pipe engineering design," European Circular Energy-Frontier Collider Study. EuroCirCol-P2-WP4-D4.3, Geneva, Switzerland, 2017.

[7] C. Garion, *FCC-hh beam screen design and prototyping,* Frascati, 09th WP4 Meeting, EuroCirCol, March 2018.

[8] S. Arsenyev and D. Schulte, "Broadband impedance of pumping holes and interconnects in the FCC-hh beamscreen," in *IPAC 2018,* Vancouver.

[9] R. Valizadeh, O. Malyshev, S. Wang, T. Sian, M. Cropper and N. Sykes, "Reduction of Secondary Electron Yield for E-cloud Mitigation by Laser Ablation Surface Engineering," *Applied Surface Science,* vol. 404, 2017.

[10] S. Calatroni, E. Garcia-Tabares, H. Neupert, V. Nistor, A. T. Perez Fontenla, M. Taborelli, P. Chiggiato, O. Malyshev, R. Valizadeh, S. Wackerow, S. Zolotovskaya, W. Gillespie and A. Abdolvand, "First accelerator test of vacuum components with laser-engineered surfaces for electron-cloud mitigation," *Phys. Rev. Accel. Beams,* vol. 20, no. 11, p. 113201, 2017.

[11] E. L. Francesca, A. Liedl, M. Angelucci, L. Gonzalez, I. Bellafont, A. Sokolov, M. G. Sertsu, F. Schäfers and R. Cimino, "Reflectivity and Photo Yield measurements of Laser treated sample," *to be published.*

[12] F. Pérez, P. Chiggiato, O. Malyshev, R. Valizadeh, T. Sian and R.Sirvinskaite, "Proposal on surface engineering to mitigate electron cloud effects.," European Circular Energy-Frontier Collider Study. EuroCirCol-P2-WP4-M4.4, Geneva, Switzerland, 2017.

[13] R. Kersevan and M. Ady, "Molflow+ and Synrad+ website," CERN, 2018. [Online]. Available: cern.ch/molflow.

[14] L. Mether and G. Rumolo, *Electron cloud,* Amsterdam, Netherlands: Conference presentation, FCC Week 2018.

[15] O. Gröbner, *Dynamic outgassing, CERN-OPEN-2000-275,* CERN, 1999.

[16] O. B. Malyshev, R. Calder, O. Gröbner, A. G. Mathewson, V. V. Anashin and A. Dranichnikov, "Synchrotron radiation induced gas desorption from a Prototype Large Hadron Collider beam screen at cryogenic temperatures," *Vacuum Science & Technology A: Vacuum, Surfaces, and Films,* vol. 14, no. 4, pp. 2618-2623, 1996.

[17] V. Baglin, "Measurement of the primary phodesorption yield at 4.2 K, 77 K and room temperature in a quasi-closed geometry," CERN. LHC-Project-Report-9, Geneva, Switzerland, 1996.

[18] J. Gómez-Goñi, O. Gröbner and A. G.Mathewson, "Comparison of photodesorption yields using synchrotron radiation of low critical energies for stainless steel, copper, and electrodeposited copper surfaces," *Journal of Vacuum Science & Technology A: Vacuum, Surfaces, and Films*, vol. 12, no. 4, pp. 1714-1718, 1994.

[19] O. S. Brüning, P. Collier, P. M. S. Lebrun, R. Ostojic, J. Poole and P. Proudlock, LHC Design Report, vol. Chapter 12, Geneva, Switzerland: CERN, 2004.

[20] V. Anashin, O. Malyshev, R. Calder and O. Gro, "Study of the photodesorption process for cryosorbed layers of H2, CH4, CO or CO2 at various temperatures between 3 and 68 K," *Vacuum*, vol. 53, p. 269, 1999.

[21] O. Dominguez and F. Zimmermann, "Benchmarking electron-cloud simulations and pressure measurements at the LHC," *AIP Conf. Proc. C*, vol. 1206051, pp. 79-83, 2013.

[22] L. Mether and G. Rumolo, *Electron cloud progress - intermediate results for beam screen design*, Geneva, Switzerland: General FCC-hh design meeting, CERN, 2017.

[23] A. Sokolov, F. Eggenstein, A. Erko, R. Follath, S. Künstner, M. Mast, J. S. Schmidt, F. Senf, F. Siewert, T. Zeschke and F. Schäfers, "An XUV optics beamline at BESSY II," in *Proceedings of SPIE - The International Society for Optical Engineering*, 2014.

[24] V. Baglin, I. R. Collins and O. Gröbner, "Photoelectron Yield and Photon Reflectivity from Candidate LHC Vacuum Chamber Materials with Implications to the Vacuum Chamber Design," CERN. LHC-Project-Report-206, Geneva, Switzerland, 1998.

[25] E. L. Francesca, A. Liedl, M. Angelucci, L. Gonzalez, I. Bellafont, A. Sokolov, M. G. Sertsu, F. Schäfers and R. Cimino, *To be published*, Frascati: LNF-INFN.

[26] O. Malyshev and I. R Collins, "Dynamic Gas Density in the LHC Interaction Regions 1&5 and 2&8 For Optics Version 6.3," LHC-project note - 274, CERN, Geneva, Switzerland, 2001.

[27] O. Malyshev and A. Rossi, "Ion desorption vacuum stability in the LHC (The multigas model)," in *7th European Conference, EPAC 2000*, Vienna, Austria, 2000.

[28] A. G. Mathewson, "Ion induced desorption coefficients for titanium alloy, pure aluminium and stainless steel," CERN-ISR-VA-76-5, CERN, Geneva, Switzerland, 1976.

[29] V. Baglin, I. Collins, O. Gröbner, C. Grünhagel and B. Jenninger, "Molecular desorption by synchrotron radiation and sticking coefficient at cryogenic temperatures for H2, CH4, CO and CO2," *Vacuum*, vol. 67, p. 421–428, 2002.

[30] L. González, M. Gil-Costa, F. Pérez, I. Bellafont, V.Baglin, P. Chiggiato, C. Garion, R. Kersevan, S. Casalbuoni and E. Huttel, "Results on the FCC-hh beam screen at the KIT electron storage ring KARA," in *9th International Particle Accelerator Conference (IPAC)*, Vancouver, Canada, 2018.

[31] L. A. González, M. Gil-Costa, I. Bellafont, V. Baglin, S. Casalbuoni, P. Chiggiato, C. Garion, E. Huttel, R. Kersevan and F. Pérez, *Results on the FCC-hh Beam Screen prototype at the KIT electron storage ring*, Amsterdam, Netherlands, FCC Week 2018.

[32] F. Pérez, L. González, S. Casalbuoni, P. Chiggiato, R. Kersevan and M. G. Costa, "Measurements of vacuum chamber at light source," European Circular Energy-Frontier Collider Study. EuroCirCol-P2-WP4-D4.2, Geneva, Switzerland, 2017.

[33] V. Anashin, A. Bulygin, O. Malyshev, L. Mironenko, E. Pyata and V. V., "Photodesorption and Power Testing of the SR Crotch-Absorber for BESSY-II," in *6th European Particle Accelerator Conference*, Stockholm, Sweden, 1998.

[34] G. Oswald, A. G. Mathewson and P. C. Marin, "Gas desorption from an oxygen free high conductivity copper vacuum chamber by synchrotron radiation photons, CERN-AT-93-12-VA," *Journal of Vacuum Science & Technology A: Vacuum, Surfaces, and Films*, vol. 12, pp. 846-853, 1994.

[35] C. Herbeaux, P. Marin, P. Rommeluère, V. Baglin and O. Gröbner, "Photon stimulated desorption of unbaked stainless-steel vacuum chambers," *Journal of Vacuum Science & Technology A: Vacuum, Surfaces, and Films*, vol. 17, no. 2, pp. 635-643, 1999.

[36] C. Foerster, H. Halama, G. Korn, M. Calderon and W. Barletta, "Desorption measurements of copper and copper alloys for PEP-II," *Vacuum*, vol. 44, no. 5, pp. 489 - 491, 1993.

[37] E. L. Francesca, A. Liedl, M. Angelucci, A. Sokolov, M. G. Sertsu, F. Schäfers, F. Siewert and R. Cimino, *Study of Reflectivity and Photo Yield on FCC-hh proposed beam screen surfaces*, FCC Week 2018, Amsterdam: LNF-INFN.

[38] R. Valizadeh, O. Malyshev, S. Wang, B.-T. Sian, M. Cropper, P. Goudket and N. Sykes, "Low secondary electron yield of laser treated surfaces of copper, aluminium and stainless steel," in *IPAC 2016*, Busan, Korea, 2016.

[39] R. Valizadeh, O. B. Malyshev, S. Wang, S. A. Zolotovskaya, W. A. Gillespie and A. Abdolvand, "Low secondary electron yield engineered surface for electron cloud mitigation," *Applied Physics Letters*, vol. 105, no. 23, p. 231605, 2014.

[40] L. Mether, *Private comunnication*, Geneva, Switzerland: CERN, 2017.

[41] F. Rieke and W. Prepejchal, "Ionization Cross Sections of Gaseous Atoms and Molecules for High-Energy Electrons and Positrons," *Phys. Rev. A*, vol. 6, no. 4, pp. 1507--1519, 1972.

12. ANNEX GLOSSARY

Acronym	Definition
BAG	Bayard Alpert Gauge
BESTEX	BEam Screen Testbench EXperiment
BS	Beam Screen
ESD	Electron stimulated desorption
FCC	Future Circular Collider
FCC-hh	Hadron Collider within the Future Circular Collider study
ISD	Ion stimulated desorption
KIT	Karlsruhe Institute of Technology
LASE	Laser ablation surface engineering
LHC	Large Hadron Collider
MB	Dipole, bending magnet
MDY	Molecular desorption yield
MM	Molecular mass
MQ	Quadrupole, focusing magnet
PSD	Photon stimulated desorption
PY	Photoelectron yield
RGA	Residual Gas Analizer
RT	Room temperature
SEY	Secondary Electron Yield
SR	Synchrotron Radiation
SS	Stainless Steel
SSS	Short straight section
UHV	Ultra High Vacuum